ION

Decimeter Positioning in an Urban Environment Through a Scalable Optical-Wireless Network

Christian Tiberius[1] | **Gerard Janssen[2]** | **Jeroen Koelemeij[3]** | **Erik Dierikx[4]** | **Cherif Diouf[1]** | **Han Dun[1]**

[1] Department of Geoscience and Remote Sensing, Delft University of Technology, the Netherlands

[2] Department of Microelectronics, Delft University of Technology, the Netherlands

[3] Vrije Universiteit Amsterdam, the Netherlands

[4] VSL National Metrology Institute, the Netherlands

Correspondence
Christian Tiberius
Faculty of Civil Engineering and Geosciences, TU Delft
Stevinweg 1, 2628 CN DELFT
The Netherlands
Email: c.c.j.m.tiberius@tudelft.nl

Abstract

This paper presents a terrestrial networked positioning system that obtains a reliable time reference from a national time scale realization and distributes it in a prototype to six roadside base stations through a fiber-optic Gigabit Ethernet network. Wireless wideband signals are transmitted by the base stations, thereby enabling positioning by a mobile receiver with an accuracy of one decimeter in a multipath urban environment. The scalability and compatibility of this system with existing telecommunication-network technologies paves the way for wide-area global navigation satellite system-independent back-up systems for timing and positioning with improved coverage and performance. The results presented in this paper are based on research carried out within the scope of a project funded by the Dutch Research Council (NWO, project 13970).

Keywords

optical synchronization, terrestrial PNT system, wideband radio ranging signal

1 | INTRODUCTION

While global positioning systems (GPSs) play a significant role in modern life, they are far from perfect. GPSs and global navigation satellite systems (GNSSs) in general are critical assets for three-dimensional positioning, navigation, and timing (PNT) worldwide. GPSs have built a remarkable track-record since their inception, meeting set performance standards and achieving impressive up-times. GPSs have become a very popular PNT sensors in a large variety of applications, including vital functions such as sustainable energy grids, telecommunication networks, and electronic banking and trading, as well as aviation, logistics and transportation, and unmanned vehicle applications. However, GPSs have several shortcomings and vulnerabilities. Typically, GPSs perform worst where they are needed most, i.e., in densely-built urban areas. In these areas, satellite signals are frequently blocked by objects that are abundantly present in these environments. This may lead to a denial of its PNT functionality. Also, signals are frequently reflected by these objects; these detoured signals are received instead of or immediately adjacent to direct line-of-sight (LoS) signals, thereby degrading its PNT performance. In addition, several authorities have expressed increasing concern about the reliance of

many other technologies and systems on GPS and GNSS signals (Sadlier et al., 2017). Several possible causes of GPS service interruption, ranging from natural disasters such as solar storms to (un)intentional jamming of GPS receivers have been identified (The Royal Academy of Engineering, 2011). While a resilient GPS back-up system with equivalent performance is urgently needed, none are currently widely available.

1.1 | A Complement to GPS

In this paper we propose a local or regional complement to GPS/GNSS for use in those areas where it is needed most. The two key components of the proposed terrestrial radio PNT system are (1) an optical infrastructure for the distribution of time and frequency reference signals across the transmitters that can be used to achieve accurate time synchronization and (2) a wideband radio signal for ranging, which effectively brings improved resistance to multipath through increased time resolution compared to narrowband signals. The developed prototype system has a set-up that is quite similar to GPS/GNSS; it includes synchronized radio-transmitters and an asynchronous mobile user receiver to deliver PNT based on the one-way signals received from the transmitters. The architecture of the system also resembles those of mobile telecommunication networks, which suggests the possibility that terrestrial PNT might be integrated into the mobile telecommunication infrastructure. The goal is to provide a glimpse of a future in which the mobile network provides not only connectivity, but also position and time information with performance beyond that currently provided by GPS devices.

1.2 | Synchronization

As alternatives to GPS satellites equipped with atomic clocks, there are several terrestrial systems such as Locata, which uses a network of radio transmitters (actually transceivers at known positions) that are capable of receiving and synchronizing each other's radio signals over the air (Barnes et al., 2003). Transceivers for ultrawideband (UWB) radios perform two-way ranging (Decawave, 2020), thus no system-level synchronization is needed. Recently, Prager et al. (2020) proposed over-the-air sub-nanosecond synchronization using 50 MHz of bandwidth by exploiting two-way time transfer (TWTT). Alternatively, an infrastructure-based time-difference-of-arrival (TDoA)-approach can be used, where the user is only transmitting and sends a short signal burst that will be received by transceivers in the infrastructure (anchors) that synchronize periodically over-the-air (Pozyx, N.V., 2020).

Transmitters can also be synchronized by coaxial cables or twisted-pair transmission lines. While distances of tens to hundreds of meters can be covered, coaxial cables suffer from temperature-dependent attenuation and low-pass filter behavior, both of which increase with distance (Bigler et al., 2018). As simultaneous two-way communication over coaxial cables is needed for calibration and compensation, appropriate implementation is not a trivial matter (Widrow, 2016). It may be necessary to revert to time-multiplexing.

Fiber-optic connections also have several advantages over electrical connections for time and frequency transfer. Optical fibers support long-distance, high-bandwidth signaling using modulated monochromatic optical carrier waves produced by lasers and can achieve baseband frequencies of over 100 GHz.

Optical attenuation of signals with wavelengths of 1.5–1.6 μm can be decreased to values as low as 0.2 dB/km and spans of tens of kilometers can be covered without signal regeneration. Optical regenerators and amplifiers permit transmission over even longer distances (up to the intercontinental scale). Fiber-optic cables, especially those in underground installations, are relatively quiet. This is because the optical phase noise caused by mechanically- and thermally-induced optical path length variations is typically less than the noise added in the electrical signal processing chain after optical-to-electrical conversion. However, the low-frequency portion of the fiber-optic noise spectrum may lead to delay variations of many nanoseconds (Dierikx et al., 2016). These variations can be accurately measured and compensated using two-way (also known as round-trip) delay measurements of optical signals propagating over the same optical fibers. The same round-trip delay measurements can also be used to estimate the one-way propagation delay with an uncertainty on the order of 10 ps (Śliwczyński et al., 2013); (Sotiropoulos et al., 2013). This implies that time and frequency transfer is possible using fiber-optic communication so that a remote clock can be made to run synchronously with a reference clock to within a few tens of picoseconds even if the two clocks are separated by a distance of hundreds of kilometers.

The terrestrial radio positioning system described in this paper relies on fiber optic time and frequency transfer for synchronization of the transmitters. Fiber infrastructure used for data-communication is typically already in place in most built-up and urban areas at places that are exactly where they need to be to complement GPS. The implementation is based on the White Rabbit network timing protocol, which combines signals for sub-nanosecond time and frequency transfer and digital communication (Gigabit Ethernet) over the same fiber within a single wavelength channel in which signal synchronization requires comparatively little capacity.

1.3 | Wideband Radio

High accuracy ranging and positioning by means of radio signals at a given signal-to-noise ratio and assuming Nyquist sampling requires a large bandwidth in the radio frequency spectrum (Kay, 1993). In a matched filter receiver, a radio signal will yield a correlation peak for time delay estimation of a width that is inversely proportional to the signal bandwidth. This will result in a wideband signal that offers high precision ranging and the capacity to identify reflections separately from the desired LoS signal. This permits precise, unbiased time delay estimation even in a dense radio multipath environment.

In GPS/GNSS, the pseudorange code measurement precision depends on the modulation chip-duration (Teunissen & Montenbruck, 2017); (Morton et al., 2021) and the chip-duration is linked reciprocally to the signal bandwidth. GPS/GNSS signals are typically used at bandwidths of a few MHz to tens of MHz at most. Locata uses signals of similar bandwidth as GPS/GNSS with a 10 MHz chipping rate pseudo-random noise (PRN) code on a 2.4 GHz carrier frequency (Barnes et al., 2005).

UWB signals employ a very wide band in the radio frequency spectrum, typically 500 MHz or more. Impulse-radio (IR) UWB is frequently used (Guvenc et al., 2006); (Yavari & Nickerson, 2014) with pulse duration typically ranging from tenths of a nanosecond to several nanoseconds. The combination of a large bandwidth and a short pulse duration offers good immunity to multipath effects, and thus permits decimeter-range accuracy (Kulmer et al., 2017); (Ruiz & Granja, 2017).

Time delay estimations with UWB signals are commonly based on energy detection and/or sub-Nyquist sampling (Guvenc et al., 2006). While optimal signal detection based on a matched filter is possible in principle, this will require very high sample rates and related computational power at the receiver. Furthermore, such a large part of the radio spectrum, in frequencies that permit propagation distances from tens to several hundreds of meters, is not freely available; thus, these signals are likely to be transmitted at very low power levels.

The terrestrial radio positioning system presented in this paper relies on wideband radio. The prototype device currently uses a bandwidth of 160 MHz centered at a frequency of 3.96 GHz that is close to the Citizens Broadband Radio Service (CBRS) band for 5G in the United States. Instead of using a single-band signal, a multi-band signal can be used that consists of several relatively narrowband signals, each 10 or 20 MHz wide, that are transmitted simultaneously. These sub-band signals can be sparsely dispersed over a much wider virtual bandwidth. This approach will facilitate (to a large extent) the high time resolution offered by this wide bandwidth while occupying only a fraction of the entire wide band. This approach was discussed previously in Dun et al. (2019) and Kazaz et al. (2021). Similarly, spectral resources are needed only for a fraction of the time. Ranging and positioning signals can be transmitted in a low duty cycle (e.g., a short burst-like packet transmitted every millisecond). Apart from the completely GPS/ GNSS-independent operation offered by an optical time and frequency transfer infrastructure, a local or regional terrestrial radio-positioning system can receive much higher signal power compared to space-borne systems such as GPS and GNSS. In addition to a much larger bandwidth, a terrestrial positioning system is much more resistant to jamming, interference, and spoofing. In addition, adverse radio signal propagation effects that occur in space and the Earth's atmosphere due to solar storms can be avoided.

1.4 | Outline of the Paper

The proposed terrestrial wireless positioning system with transmitters that are synchronized through a fiber-optic Ethernet network will be presented in Section 2. Section 3 discusses the optical time-frequency distribution including the architecture of the prototype deployed on the Delft University of Technology campus and presents synchronization results obtained with the prototype. Section 4 focuses on wideband ranging and considers the architecture of radio transmitters and the receiver in the prototype system. The ranging signal, time delay estimation, and the positioning model are also detailed here. Finally, positioning results obtained with the prototype are presented in Section 4.5. Section 5 discusses the implementation and deployment of the system in practice, and Section 6 presents the main conclusions of this work.

1.5 | Earlier Work

Aspects of this research project have been published previously, including presentations at several of ION conferences (Dun et al., 2019); (Diouf et al., 2020). The full concept of the system together with positioning results obtained with the prototype were also published previously (Koelemeij et al., 2022). A popular article that briefly outlined the system concept and summarized the results was also recently published (Diouf et al., 2022).

2 | TERRESTRIAL NETWORKED POSITIONING SYSTEM: CONCEPT

The basic concept underlying the terrestrial networked positioning system (TNPS) is shown schematically in Figure 1. The TNPS resembles GPS in the sense that it relies on the transmission of wireless ranging signals which are synchronized to atomic clocks. A mobile user receiver can combine ranging signals from multiple transmitters and, together with information about the transmitter positions, determine its own position. The proposed terrestrial positioning system is implemented somewhat differently. Instead of space-borne vehicles with on-board atomic clocks, the system uses terrestrial transmitters, e.g., those placed on a grid with city-block-sized spacing. Each transmitter is equipped with a (low-cost) oscillator which can be synchronized to a common reference time scale through a fiber-optic network. The optical network functions as a distributed (atomic) time scale realization to which an arbitrary number of transmitters can be connected. In the proposed system, fiber-optic propagation delays between each transmitter and the reference time scale are accurately measured and corrected so that each transmitter replicates the reference time scale within a small fraction of a nanosecond (as described further in Section 3). To mitigate the detrimental effects of multipath, the radio transmitters employ wideband signals (see Section 4). As we show here, the combination of wideband signals and sub-nanosecond time synchronization facilitates decimeter level accurate positioning in multipath environments; an equivalent GPS/GNSS receiver would perform at an accuracy of many meters (Braasch, 2017). Likewise, mobile receivers can synchronize their local oscillators over-the-air to the terrestrial positioning system and thus obtain the atomic reference time with sub-nanosecond accuracy. This can be compared with the 10–30 nanosecond accuracy provided by a GPS timing receiver (Defraigne, 2017).

The proposed system architecture provides advantages based on the dependability of PNT signals. Owing to the vicinity of local terrestrial transmitters, mobile users can benefit from much stronger wireless signals which are far less susceptible
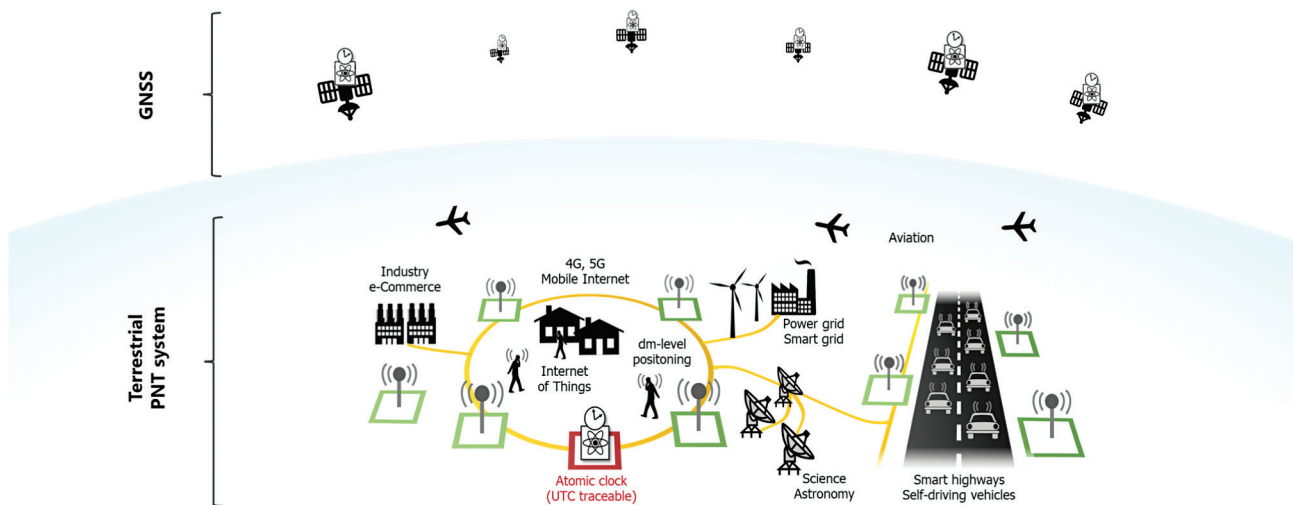

FIGURE 1 TNPS compared to a GNSS with several possible applications. Yellow lines represent fiber-optic connections. Green squares represent terrestrial wideband radio transmitters that are time-synchronized over fiber-optic connections. In areas where no fiber-optic connections are available, auxiliary transmitters, for example, those seen at the right side of the highway, can be synchronized over-the-air to increase coverage and PNT precision.

to interference or jamming than GPS signals, which may be easily overwhelmed in a wide area by a single jammer. This feature improves the resilience of positioning and timing applications. Furthermore, sub-nanosecond time distribution represents a disruptive step forward in the fiber-optic network compared to previous time-distribution technologies. Examples include the Network Time Protocol (NTP) and the Precision Time Protocol (PTP, IEEE 1588) which provide time with millisecond (NTP) and (sub-)microsecond accuracy (PTP). In the next Section, we describe the fiber-optic time distribution technology employed using White Rabbit.

3 | OPTICAL TIME-FREQUENCY DISTRIBUTION

3.1 | White Rabbit

The White Rabbit (WR) network timing protocol is a unique fiber-optic time and frequency transfer method that was originally developed as a beam-timing system and deterministic control network for the Large Hadron Collider at CERN (Serrano et al., 2009); (Moreira et al., 2009). WR is an evolution of the IEEE 1588 Precision Time Protocol and ITU Synchronous Ethernet (SyncE) protocol and is included as the High Accuracy profile of the 2019 version of the IEEE 1588 standard. To the best of our knowledge, WR is currently the only technology which combines signals for sub-nanosecond time and frequency transfer and digital communication (Gigabit Ethernet) within a single wavelength channel. WR is commercially available as open-source Ethernet equipment, including switches and nodes. Users can build fiber-optic Ethernet networks in which each WR device replicates the time and frequency of a single reference time scale realization typically based on atomic clocks. To this end, the reference time scale realization feeds its time and frequency signals into a WR device set up in grandmaster mode and will act as the time source for the entire WR network, as shown in Figure 2. WR connections are inherently hierarchical; WR master devices transfer the reference time and frequency to downstream WR slave devices (Serrano et al., 2009). WR devices often act both as a slave and a master, and therefore have multiple optical ports. In this case, one port is used to enslave the WR device to an upstream WR master device,
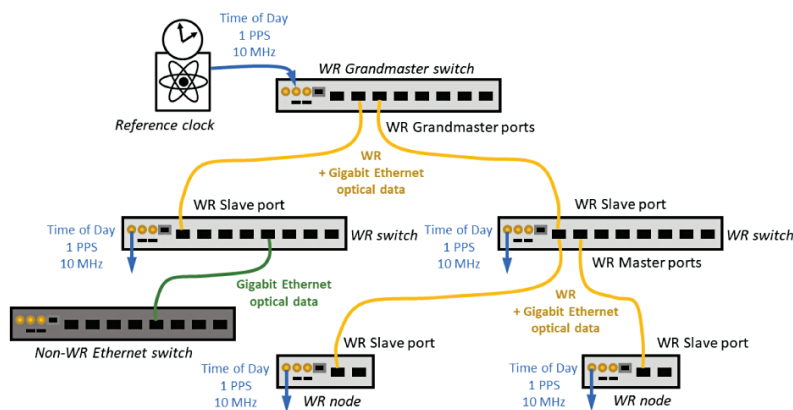

FIGURE 2 Simple example of a White-Rabbit (WR) network lay-out. WR-compatible Ethernet switches facilitate the development of complex network topology combined with regular Gigabit Ethernet networking, along with the distribution of time and frequency signals produced by a reference (atomic) clock. Both WR switches and low-cost WR nodes can be used to synchronize PNT transmitters. Yellow and green lines represent fiber-optic connections and interfaces; electrical connections and interfaces are shown in blue.

while other ports can be configured as master ports to which multiple downstream WR slave devices are connected. Complex network topology with thousands of nodes are possible and fail-safe redundant connections have been demonstrated (Lipinski, 2016).

When estimating the one-way delay from a round-trip delay measurement, the path is assumed to be symmetric in both the upstream and downstream directions. In practice, large (nanosecond-level) delay asymmetries occur. These can be identified and corrected as follows. First, asymmetrical delays between the transmitting and receiving paths inside WR devices and optical transceivers are calibrated once, prior to their installation into the network (Daniluk, 2015), (Peek & Jansweijer, 2018). WR employs bidirectional communication using two different wavelengths propagating over the same (single) fiber for precise round-trip delay measurements. The physical length of the fiber-optic path is therefore inherently symmetrical. However, chromatic dispersion in the optical fiber leads to a delay asymmetry which, if left uncompensated, could lead to timing errors at the nanosecond level. Thus, the WR calibration procedure also includes a calibration of the fiber delay asymmetry at the time of installation (Daniluk, 2015). Once operational, each pair of WR devices (master and slave) automatically performs quasi-continuous measurements of the round-trip delay over the fiber. The one-way propagation delay (and its variations) is then determined and compensated electronically with a control bandwidth of 30 Hz. Thus, the one-way delay is tracked continuously and timing noise caused by random path length variations of the optical fiber is suppressed within the control bandwidth.

With all delays measured and corrected, the time, phase and frequency derived from a low-cost local oscillator in the downstream WR slave device can be locked to those of the upstream WR master device. To this end, the quasi-periodic symbol changes in the 1.25 Gb/s bitstream are used as a transfer oscillator. This facilitates a phase-lock between two WR devices and allows the local oscillator of the WR slave device to replicate the time, phase, and frequency of the reference time scale realization with very little additional degradation of stability or accuracy. At each WR device, time and frequency are available both digitally (in the form of IEEE 1588 time stamps) and electrically from coaxial 1 pulse per second (PPS)/10 MHz output ports. The signals provided through these output ports are fully phase-coherent with the signals from the WR grandmaster and the reference time scale.

WR has been shown to be compatible with optical amplifiers and the existing long-distance fiber-optic telecommunication infrastructure carrying live data traffic (Dierikx et al., 2016); (Boven et al., 2019); (Dierikx et al., 2019). A residual time offset between WR devices of 0.4 ns was demonstrated over a distance of 169 km (Boven et al., 2019). This performance, together with the compatibility of WR with the existing fiber-optic infrastructure (see also Section 5) and the high scalability of its networks, makes WR a promising candidate for the creation of a ubiquitous time and frequency reference network. Specifically, WR can feed wideband terrestrial transmitters with accurate time signals so that a positioning accuracy of one decimeter can be achieved for a mobile user. Moreover, if the reference time is taken from a time scale realization designated by a national metrology institute or national time laboratory, as demonstrated in this paper, the network could simultaneously disseminate an approximation of the coordinated universal time (UTC) and the SI second independent from GPS, potentially with higher accuracy, to mobile users.

The residual time offset and time stability (TDEV) typically achieved using default WR gear (similar to the equipment used in this paper) are approximately a few 0.1 ns and 10 ps, respectively, over 200 s or longer (as discussed in the Subsection to follow). This satisfies the needs of ranging and positioning by means

of time delay (pseudorange) measurements, which is another focus of this paper. Given appropriate hardware modifications, these figures may be reduced to below 0.1 ns and 1 ps, respectively (H. Li et al., 2015); (Rizzi et al., 2016); (Rizzi et al., 2018). This places lower bounds on the achievable accuracy and reproducibility of carrier-phase ranging to 3 cm and 0.3 mm, respectively. Further improvements can be expected once purely optical time and frequency transfer methods are implemented, which may be capable of delivering time with femtosecond-level stability and accuracy (Bergeron et al., 2019).

3.2 | TNPS-Prototype Synchronization Architecture

A prototype TNPS has been deployed at The Green Village on the TU Delft campus (Figure 3). This site is only a few kilometers away from the Dutch National Metrology Institute, VSL, home of the Dutch National Time Scale, UTC(VSL). With support from the collaborative organization for ICT in Dutch education and research known as SURF, an optical fiber connection was arranged for the White Rabbit synchronization network between VSL and TU Delft. This network is set up as a loop that returns from TU Delft back to VSL, and thus enables monitoring
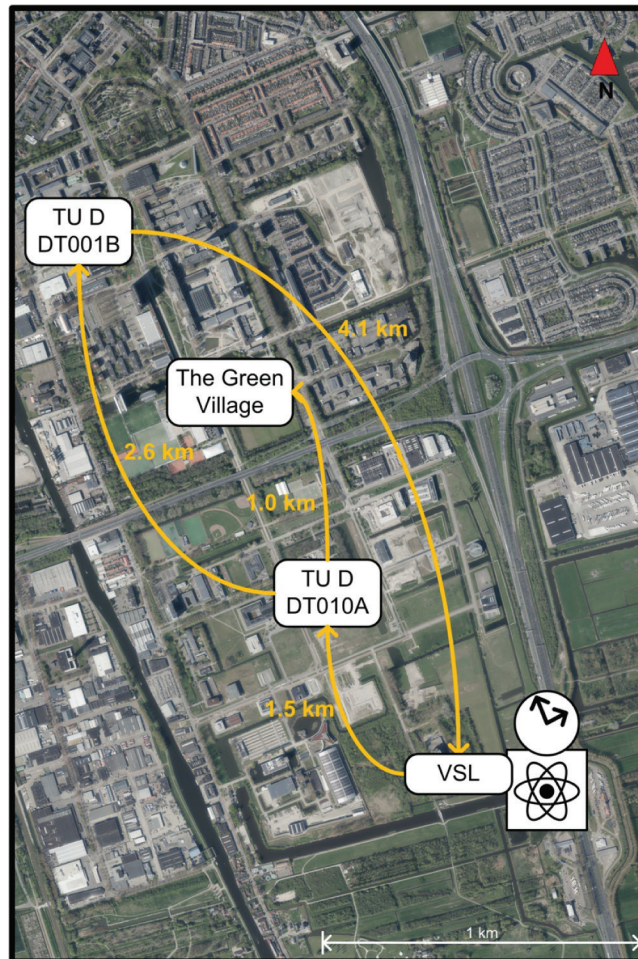

FIGURE 3 Geographical representation of the synchronization network, with time and frequency reference signals from UTC(VSL). An aerial photograph that features the southeastern part of the town of Delft and the TU Delft campus was obtained through Beeldmateriaal Nederland under a CC BY 4.0 license (Beeldmateriaal Nederland, 2021).

of the synchronization stability. At the TU Delft campus, the loop includes two data centers identified as DT010A and DT001B. A WR link was established from data center DT010A to The Green Village using the existing TU Delft optical fiber infrastructure. A geographical representation of the setup is shown in Figure 3 and a schematic diagram of the synchronization infrastructure of the prototype system is shown in Figure 4.

Each link in the WR network consists of a single mode fiber. Two wavelengths are used for transfer of WR synchronization packets between the master and slave device with one wavelength in each direction. In our implementation, WR traffic is separated from other traffic in the network with coarse wavelength division multiplexing (CWDM) filters, shown by the trapezoid symbols in gray in Figure 4 that are applied in the links that connect the sites at different geographic locations. The internal delays of these CWDM filters were calibrated before installation. The wavelengths between the sites were chosen to be close together (typically separated by only 20 nm) to minimize delay asymmetries introduced by chromatic dispersion over longer distances.

At The Green Village, the WR timing nodes are connected in a a pattern known as a daisy chain. In this pattern, each node is synchronized to the previous one in a master-slave pair. This daisy chain arrangement, unlike the lay-out of the WR network shown in Figure 2, was chosen based on equipment that was available at the time of the experiment. In this part of the network, there is no other traffic in the fibers and thus no WDM filters were used. Here, although the wavelength separation is 180 nm, the effect of delay asymmetry remains small because of the short optical fiber lengths of only 50 m between the WR timing nodes.

At VSL, the WR Grandmaster (WR-GM) is directly referenced to the national timescale realization UTC(VSL). Because of cable and internal hardware delays, the time broadcast by the WR-GM is delayed with respect to UTC(VSL) by 97 ns with an uncertainty of 1 ns root mean square error (RMSE). In this section, we quantify uncertainty in terms of the RMSE, taking into account both random spread (precision) and systematic effects (biases), if any.

The WR slave (WR-SL) at VSL is delayed with respect to UTC(VSL) by 91 ns with an uncertainty of 1 ns (RMSE). This means that the offset introduced by the WR
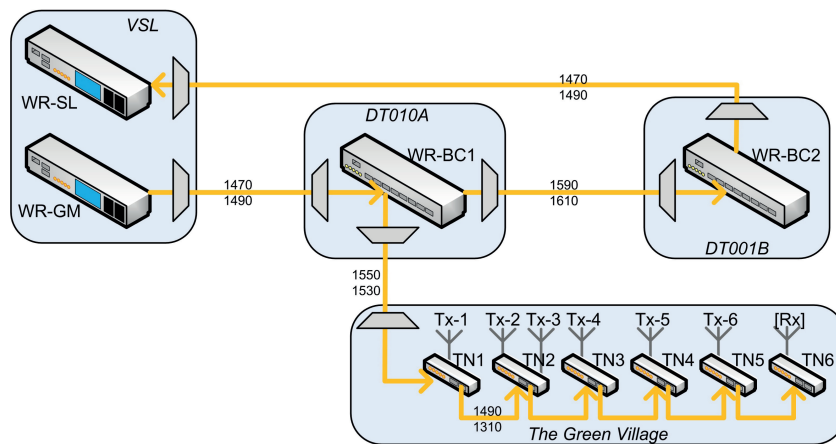

FIGURE 4 Schematic diagram of the WR optical synchronization infrastructure. The infrastructure starts at the WR Grandmaster (GM) at VSL and leads to the WR switch (Boundary Clock – BC1) at one of the data centers. It then arrives at the WR timing nodes (TNs) at the experiment site of The Green Village. The loop runs from WR Grandmaster (GM), through the two WR switches (Boundary Clocks BC1 and BC2) and back to WR Slave (SL) again at VSL. The optical wavelengths for each connection are as indicated (in nm).

link "WR-GM(VSL) - WR-BC1(DT010A) - WR-BC2(DT001B) - WR-SL(VSL)" is about 6 ns. (Note that both WR-GM and WR-SL are WR-ZEN TP, and both WR-BC1 and WR-BC2 are WRS-3/18, all by Seven Solutions). Based on calibration of the WDM filters, these asymmetries introduced an offset of 3 ns. The estimated offset introduced by fiber delay asymmetry caused by chromatic dispersion was 1 ns. The remaining offset of 2 ns was most probably caused by internal delay asymmetries in the WR devices in this loop. While these were not calibrated prior to the installation of the equipment, a fixed unknown time offset from the reference time scale is not critical for the operation of the TNPS prototype.

The link between switch WR-BC1(DT010A) and timing node TN1 (at The Green Village), is approximately 1 km. With the wavelengths selected close together, the offset introduced by fiber delay asymmetry caused by chromatic dispersion was estimated to be less than 1 ns. Because the WDM filters and internal delays of the WR devices in this link were not calibrated, this link introduces an unknown offset.

For the purpose of positioning with the TNPS prototype, the most critical part is the synchronization of the WR timing nodes located at The Green Village with respect to one another (rather than to the reference timescale). These TNs, by OPNT, are the basis for synchronized transmission of the ranging signals. Therefore, in the VSL laboratory, the internal delays of these WR timing nodes were calibrated for each pair of interconnected nodes by relative calibration (Daniluk, 2015).

In this method, by first order approximation, it is assumed that the sum of internal transmitter (Tx) and receiver (Rx) delays in the master and slave devices are equal. From the round-trip time measurement, the delay of the short fiber used in the calibration is eliminated. This result divided by 2 provides an estimate of the sum of internal Tx and Rx delays in each device. Furthermore, also as a first approximation, it is assumed that the internal Tx delay is the same as the internal Rx delay. Thus, the initial calibration parameters for the Tx and Rx delay in the WR timing nodes are set to the measured round-trip time minus the delay of the fiber, divided by 4.

With these initial settings, the time difference between the 1 PPS output from the WR master and the 1 PPS output from the WR slave can be measured with a time interval counter. Based on the reading of the time interval counter, the Tx and Rx calibration parameters can be iteratively fine-tuned until the 1 PPS difference becomes less than 0.1 ns. This is typically achieved after two iterations. Ideally, for high-precision applications of TNPS, even better synchronization would be desired. However, with the current generation of WR equipment the stability, repeatability and 1 PPS pulse shape do not lead to better performance.

3.3 | TNPS-Prototype Synchronization Results

After relative calibration of the WR timing nodes in the VSL laboratory, five of the timing nodes were mounted in weather-proof boxes together with the transmitters and installed on site in lamp-posts (see Section 4.2). The sixth timing node was incidentally set up with the mobile receiver to synchronize it for the purpose of validation of an additional over-the-air time and frequency transfer experiment.

During the experiments with the prototype system, an on-site verification of the synchronization of the WR timing nodes was performed. This verification included two steps: (1) measurement of the absolute time offset between WR-TN1 and UTC(VSL) and (2) measurement of the synchronization between WR-TN1 and the other timing nodes locally at The Green Village. Finally, the time and frequency stability of the WR optical synchronization infrastructure was analyzed.

3.3.1 | Absolute time offset

For the TNPS prototype demonstration at The Green Village, the absolute time offset of WR-TN1 with respect to the reference time scale, UTC(VSL), is not critical. Nevertheless, to verify that WR-TN1 was properly locked to the WR grandmaster, the time offset was measured by means of a portable clock based on a rubidium oscillator. This portable clock was synchronized to UTC(VSL) in the VSL time laboratory, and then carried to The Green Village while under battery power. The verification revealed that WR-TN1 was properly locked to the WR grandmaster at VSL, and WR-TN1 was delayed with respect to UTC(VSL) by 24 ns with an uncertainty of 50 ns (RMSE).

3.3.2 | Synchronization of timing nodes

The synchronization of the local network of WR timing nodes, which was of critical importance to the positioning functionality of the prototype system, was verified with an SR620 time interval counter. The 1 PPS output of each of the WR-TN2 to WR-TN6 was compared to the 1 PPS output of WR-TN1, while all six timing nodes were synchronized in a daisy chain (Figure 4). WR-TN1 was synchronized to switch WR-BC1 at DT010A. Both timing nodes were connected to the time interval counter with cables of approximately equal (30 m) length. The cable and counter offsets were determined before the verification measurements and were corrected as shown in Table 1.

The estimated uncertainty in these measurements was 0.5 ns RMSE. The results shown in Table 1 reveal that the remaining time offsets between the nodes are small. All offsets are less than or equal to the uncertainty.

3.3.3 | Stability analysis

The stability of time and frequency of the WR optical synchronization network was evaluated for the loop "VSL - DT010A - DT001B - VSL" and for the daisy-chain of timing nodes at The Green Village.

Figure 5 shows the time and frequency stability expressed as time deviation (TDEV) and modified Allan deviation (MDEV), respectively (Riley, 2018), of the loop "VSL - DT010A - DT001B - VSL" measured over approximately 100 days. The TDEV is typically below 10 ps. For averaging times below 200 s, TDEV is higher and is dominated by the noise from the time interval counter.

The noise introduced by the daisy-chain of timing nodes is shown in Figure 6 and includes TDEV of the link between WR-TN1 and WR-TN2 and of the entire chain

TABLE 1

Verification of WR Timing Node Synchronization: Averages of Measured Time Differences with 0.5 ns RMSE Uncertainty.

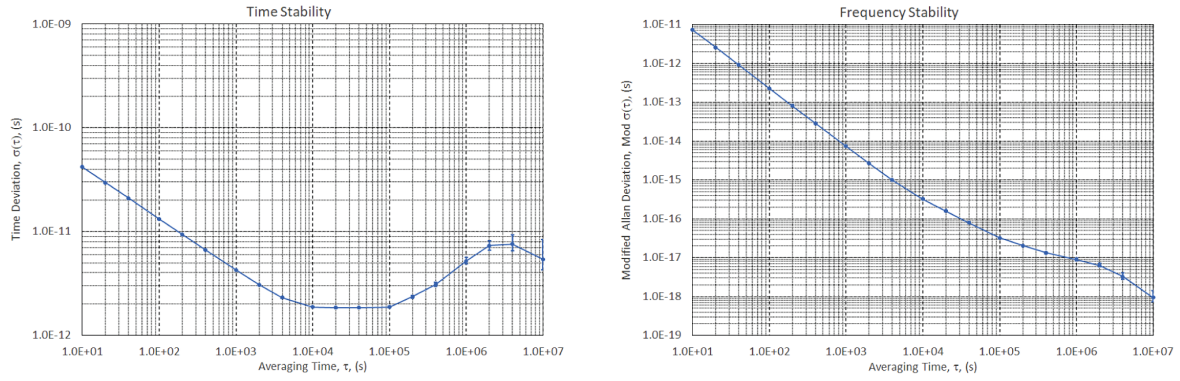| Timing nodes	1 PPS difference (ns)
TN1 - TN2	0.3
TN1 - TN3	0.5
TN1 - TN4	0.5
TN1 - TN5	0.4
TN1 - TN6	0.5

FIGURE 5 Time stability (TDEV - left) and frequency stability (MDEV - right) of the loop "VSL - DT010A - DT001B - VSL" with 1-sigma error bars. The data presented in these graphs were taken from Koelemeij et al. (2022).
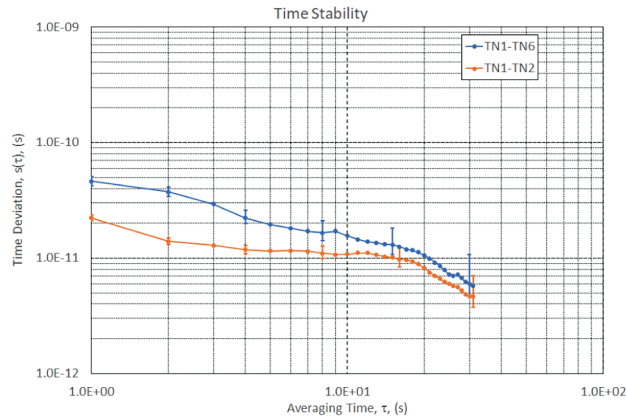

FIGURE 6 Time stability (TDEV) of the link "WR-TN1 – WR-TN2" (in orange) and the link "WR-TN1 - WR-TN2 - WR-TN3 - WR-TN4 - WR-TN5 - WR-TN6" (in blue) with 1-sigma error bars. The data presented in this graph were taken from Koelemeij et al. (2022).

from WR-TN1 to WR-TN6. The noise contribution from the daisy-chain of timing nodes is approximately a factor of 2 with respect to a single WR link between two timing nodes.

3.4 | Discussion and Outlook

The transmitters in the TNPS prototype deployed at The Green Village were synchronized with a daisy-chain of WR timing nodes. The first timing node in this chain was connected to a WR network that was synchronized with the Dutch National Timescale UTC(VSL) within approximately 100 ns, also verified here. The accuracy of the synchronization with the reference timescale might be further improved by calibration of all components in the WR network between VSL and The Green Village. In this case, synchronization within 0.5 ns can be achieved. However, for the purpose of positioning with this prototype system, the accuracy of the synchronization with the reference timescale is not critical. The synchronization of the 1 PPS outputs of the timing nodes in the daisy-chain, calibrated in the VSL Time Laboratory to a level within 0.1 ns and verified on site at The Green Village, was found to be within 0.5 ns.

In order to set-up a large network, according to the lay-out shown in Figure 2, one would deploy a cascade with WR timing nodes connected to the final level of WR switches. Cascades of up to five standard 18-port WR switches (Rizzi et al., 2018) would suffice for covering an area as large as the Netherlands, with WR timing nodes geographically separated by 500 m.

4 | WIDEBAND RADIO RANGING

In this section, we introduce the radio channel and address the impact of bandwidth of the ranging signal on time delay estimation. The architecture of the developed prototype system as well as the receiver signal processing will be outlined. After detailing the ground-truth, positioning results based on time delay estimation will be presented.

4.1 | Radio Channel and Ranging Signal Bandwidth

Typically, radio ranging is performed based on an estimation of the time duration between transmission of the ranging signal by the transmitter and arrival of this signal at the receiver. Estimation of this time delay is particularly challenging in a practical dense multipath radio channel, i.e., those with many reflections, because the receiver may mistakenly use a reflected signal for measurement instead of the desired direct-path or line-of-sight (LoS) signal. In addition, the receiver may not be able to distinguish the LoS signal from close-in reflections with a slightly longer delay. This will result in an offset (bias) in the estimated time delay of the signal.

In the following sections, we consider a baseband signal model with a ranging signal $s(t)$. The transmitted bandpass signal at frequency f_c is then given by $x(t) = \text{Re}\{s(t)e^{j2\pi f_c t}\}$, where $\text{Re}\{\cdot\}$ indicates the real part of a complex variable. For an L-path multipath channel, the channel impulse response (CIR) can be modeled as shown in Equation (1):

$$h(t) = \sum_{l=1}^{L} \alpha_l \delta(t - \tau_l),\tag{1}$$

where α_l and τ_l are, respectively, the real-valued path gain and time delay of the lth path between transmitter and receiver. The received baseband signal is then given by Equation (2):

$$\begin{aligned}\underline{r}(t) &= s(t)e^{j(2\pi f_\Delta t + \theta_0)} * h(t) + \underline{n}(t) \\ &= \sum_{l=1}^{L} \alpha_l s(t - \tau_l) e^{j(2\pi f_\Delta(t - \tau_l) + \theta_0)} + \underline{n}(t),\end{aligned}\tag{2}$$

where $*$ indicates convolution, a random variable is denoted by an underscore, e.g. $\underline{n}$, θ_0 is the phase offset between transmitter and receiver at $t = 0$, f_Δ is the frequency difference between the receiver front end and the received signal, caused by a frequency offset between transmitter and receiver and/or by a Doppler shift (both assumed constant here for convenience of the discussion), and $\underline{n}(t)$ is zero-mean Gaussian distributed noise with variance σ_n^2. For ranging, the variable of interest is the time delay τ_1 of the LoS path, with its estimate indicated as $\hat{\tau}_1$. (In this paper, we do not consider non-line-of-sight [NLoS] scenarios.) In Section 4.3.1, the time delay will be estimated via a model of the CIR. This response can be obtained as the

transmitted ranging signal $s(t)$ is *a priori* known to the receiver. The model will be formulated in the frequency domain in terms of the channel frequency response.

Without considering any reflections in the time delay estimation (i.e. assuming a single path channel), the ranging precision can be bounded by the (in practice rather optimistic) Cramer-Rao lower bound (CRLB), which defines a lower bound on the variance of the unbiased estimation error $\sigma_{\hat{\tau}_1}^2$. The CRLB for a single path LoS channel is given by Kay (1993) as shown in Equation (3):

$$\sigma_{\hat{\tau}_1}^2 \geq \frac{1}{\text{SNR}\,\mathbf{F}^2}, \tag{3}$$

and is determined by the signal-to-noise ratio (SNR) and the mean square or Gabor bandwidth $\mathbf{F}^2$ of the signal, defined as shown in Equation (4):

$$\mathbf{F}^2 = \frac{\int_{-\infty}^{\infty} (2\pi f)^2 \, |S(f)|^2 \, df}{\int_{-\infty}^{\infty} |S(f)|^2 \, df}, \tag{4}$$

where $S(f)$ is the Fourier transform of $s(t)$. Equation (4), shows that the Gabor bandwidth is related to the ranging signal bandwidth. From the time delay estimate $\hat{\tau}_1$, the estimate of the distance ρ between transmitter and receiver is found as $\hat{\rho} = c\hat{\tau}_1$, where c is the speed of light, and the variance of this range estimate thus becomes $\sigma_\rho^2 = c^2 \sigma_{\hat{\tau}_1}^2$.

To reduce the range estimation error variance, a signal with a larger Gabor bandwidth can be used and/or the SNR can be increased. As a rule of thumb, doubling the RMSE bandwidth $\mathbf{F}$ will reduce the range estimator standard deviation $\sigma_{\hat{\tau}_1}$ by a factor of 2. Figure 7 shows the difference between the ideal CIR, as measured with an infinite bandwidth signal, and the CIR when measured with a signal of limited bandwidth (as shown by the dashed line in brown).

The time resolution determines the minimum time difference in which the multipath components can still be separated. Multipath components that arrive with delays that are less than the time resolution from the LoS path will likely introduce a bias in the estimated time delay $\hat{\tau}_1$ for the LoS path. This time resolution, in case of matched filtering, is determined by the width of the correlation
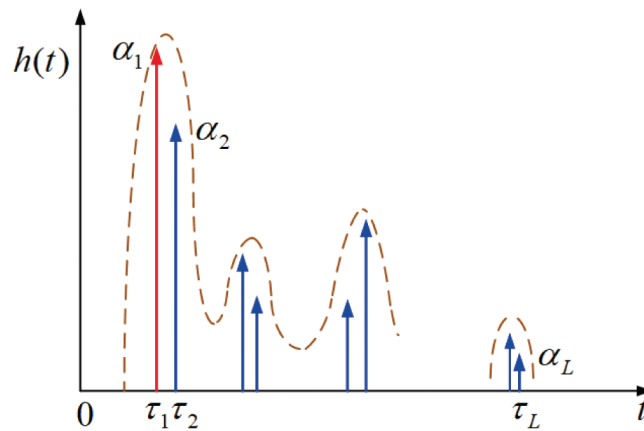

FIGURE 7 CIR measured with an infinite bandwidth signal (δ-pulses in red and blue) and with a signal of limited bandwidth (dashed line in brown). The red δ-pulse represents the LoS path ($i = 1$), α_i and τ_i represent the amplitude and delay of the i-th multipath component, respectively.

peak, which is inversely proportional to the signal bandwidth. Therefore, the precision of time delay estimation and the separability of the multipath reflections are inversely proportional to the signal bandwidth. This makes the use of wideband ranging signals essential in achieving a high ranging and positioning precision and accuracy.

With respect to the application of autonomous driving as shown in Figure 1, the automotive radio channel can be characterized as a time variant multipath channel due to reflective vehicles moving in a reflective environment that includes buildings and infrastructure and vehicles moving with respect to one another. This results in a rapidly changing CIR in which the LoS path may be blocked intermittently. In addition, the different multipath components will exhibit various Doppler shifts. When a short duration ranging signal is used, the channel can be assumed quasi-static (i.e., during the measurements for a position fix). For a vehicle moving with a speed of 150 km/h, the displacement during a ranging signal burst of 160 μs, as used here, is only 6.7 mm, as shown in Figure 9. Given this displacement, the relative phase differences between multipath components and delays will change slightly in relation to the direction of arrival and direction of movement; however, the path amplitudes will remain relatively constant.

4.2 | TNPS-Prototype Architecture

The setup of the TNPS prototype includes six transmitters (Tx-1 to Tx-6) and one receiver (Rx), which are all based on an Ettus X310 universal software radio peripheral (USRP). Each USRP has two radio frequency (RF) channels that can be configured either as transmitter or receiver channels. A transmitter consists of a USRP connected to a timing node for time-frequency synchronization. One of the USRPs operated as two independent transmitters (Tx-2 and -3). The receiver unit consists of a USRP which can operate in asynchronous mode; it can also be connected to a timing node for synchronization to the same time-frequency reference as the transmitters. In this way, the performance of over-the-air and hard-wired synchronization with a timing node can be compared. The transmitters periodically stream the ranging signals; the receiver samples the received signals, stores the samples, and forwards them to a host-personal computer (host-PC) for offline processing.

After development and initial testing in the lab, the prototype system was deployed at The Green Village. The Green Village, located on the TU Delft campus, is an outdoor living laboratory for sustainable innovation. The main goal of this facility is to accelerate development and implementation of innovations by bringing together engineers, businesses, and scientists at a place where new technologies can be developed, tested, and demonstrated (The Green Village, 2021). This site offers a realistic environment for testing the TNPS in an area with buildings and surrounding infrastructure (see Figure 8). The site offers access to the TU Delft ICT facilities with (dark) single mode fibers on site (see Section 3.2). Tests have been carried out on a 40 m stretch of a 6 m wide local paved road on which the mobile receiver can move freely, as shown in Figure 8. The transmitters are located along this road, with antennas mounted primarily on lamp-posts at a height of approximately 4 m. The lay-out of the prototype-deployment was primarily opportunity-driven (e.g., using existing lamp posts to mount transmitter antennas). Tests have been carried out with the receiver attached to a trolley and also to a car to facilitate kinematic experiments at low speed only (walking pace).

4.2.1 | *Synchronization*

The time-frequency reference signals derived from UTC(VSL) and transported to the Green Village via the optical network (Section 3 and Figure 4) were used to synchronize the timing nodes, as shown in Figure 9. The X310 USRPs use the 1 PPS and 10 MHz signals of the timing nodes (Figure 2), which are mutually synchronized and enslave its local clock and phase-locked loop (PLL) for carrier frequency generation. In this configuration, the six transmitter USRPs can trigger the transmission of the ranging signals with deterministic time delays related to the synchronized 1 PPS signal and thus with respect to each other. In practice, even after calibration of the timing nodes, there will be a residual delay uncertainty in the order of 100 ps between the 1 PPS signals provided by the timing nodes and

FIGURE 8 Prototype setup at The Green Village. Two of the transmitter antennas are visible in the lamp posts to the left (in red circles). The receiver antenna Rx (in yellow circle) is fixed to the trolley. The land-surveying stations at the right are used to provide the ground-truth trajectory of the receiver.
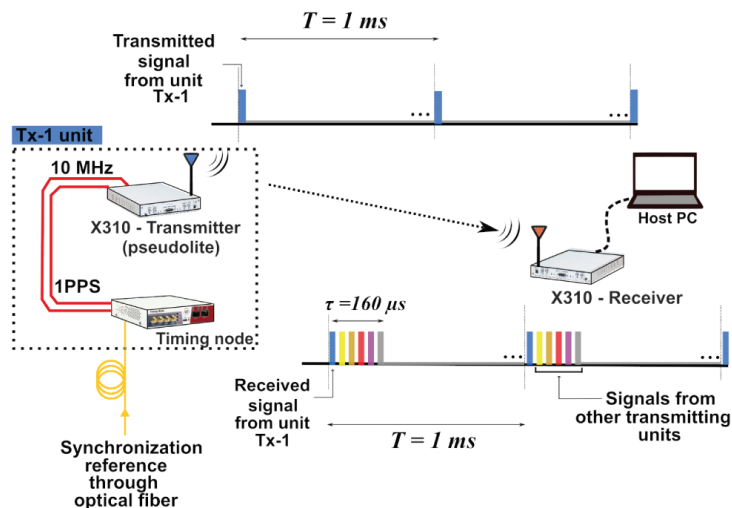

FIGURE 9 Ranging signal transmission in time division multiplex (TDM) mode. A single Tx - Rx configuration in which the time-frequency reference is provided to the timing node through the optical telecommunication network (in yellow). The timing node delivers 1 PPS and 10 MHz electrical signals (red lines) to the X310 based radio transmitters. The transmitters stream the ranging signals periodically every $T = 1$ ms in a low duty cycle scheme. The ranging burst contains the TDM ranging signals of multiple transmitters. The receiver samples the incoming ranging signals and forwards the data to the host-PC for offline processing and time delay estimation.

a residual 10 ps-level uncertainty introduced by hardware delays in each USRP RF front end. This translates, to delay differences at the 100 ps-level between the USRPs' radio transmission times.

4.2.2 | X310 USRP main features and configuration

The local sample clock of the USRP of 200 MHz was syntonized to the 10 MHz frequency reference. Signals were sampled in quadrature with a sample format of 16 bits-I (in-phase) and 16 bits-Q (quadrature-phase). The maximum effective radiofrequency (RF) bandwidth was limited to 160 MHz. Each X310 USRP has two RF channels with a central frequency that can be tuned from 10 MHz to 6 GHz. In the TNPS prototype, the USRPs are operated at a carrier frequency of 3.96 GHz based on an experimental license obtained from the Dutch Telecom Agency. The output power of a transmitter is $P_{tx}=\ +14.5$ dBm during burst transmission. The receiver gain was set to 20 dB since higher gain values impaired the received signals. At the transmitters and the receiver, identical omni-directional, ceiling mountable, wideband antennas from Taoglas are used with a gain of 3 dBi. The transmitters and receiver were connected to the antennas by cables of 5 m and 1 m, with measured cable losses of 5.6 dB and 0.9 dB, respectively. The received LoS signal power at a distance d (in meter) at the receiver-USRP input can be expressed as Equation (5):

$$P_{rx_{LoS}} = -30.4 \ \text{dBm} - 20 \log_{10}(d) \ \text{dB} \tag{5}$$

The noise level within the 160 MHz measurement bandwidth and referenced to the receiver-USRP input was measured at −80.5 dBm. The SNR, defined here as the ratio of the received signal power and received noise power before correlation, varied from = −1 dB to 34 dB over the 40 m track because of variations in both distance and multipath fading. With the receiver located at the Reference Point (Ref. Pnt.) shown in Figure 16, the SNR values of the measured bursts from Tx-1 to Tx-4 and Tx-6 (with Tx-5 deactivated) as shown in Figure 10 were 15.2, 21.7, 22.4, 17.3, and 28.7 dB, respectively. Using Equation (5), the coverage distance is $d = 320$ m for SNR = 0 dB based on the received LoS path power. This would allow the geometry of The Green Village set-up as described earlier to be scaled by a factor of 10 to fit a highway scenario.

4.2.3 | Ranging signal structure

For ranging, a bursts transmission scheme was used, in which Tx-1 to Tx-6 periodically transmitted the ranging signal every 1 ms employing a time division multiplexing (TDM) scheme, in which the respective signals were synchronized to one another (Figure 9). The duration of a TDM ranging burst can be as long as 160 μs which will result in a transmission duty cycle of 0.16. For six transmitters, the ranging burst is divided into six time slots of 24.6 μs each separated by a guard time of 2.5 μs between successive slots. In the prototype, quadrature phase shift keying (QPSK) modulated PRN sequences and orthogonal frequency division multiplex (OFDM) signals are used as ranging signals. Figure 10 illustrates the received signal bursts from the transmitters using a PRN-sequence with Tx-5 deactivated. The embedding of the ranging signal burst in an OFDM signal is shown in Figure 11. The receiver can be connected to a timing node to synchronize the receiving window with the transmitting window. Alternatively, when not connected to a timing node,
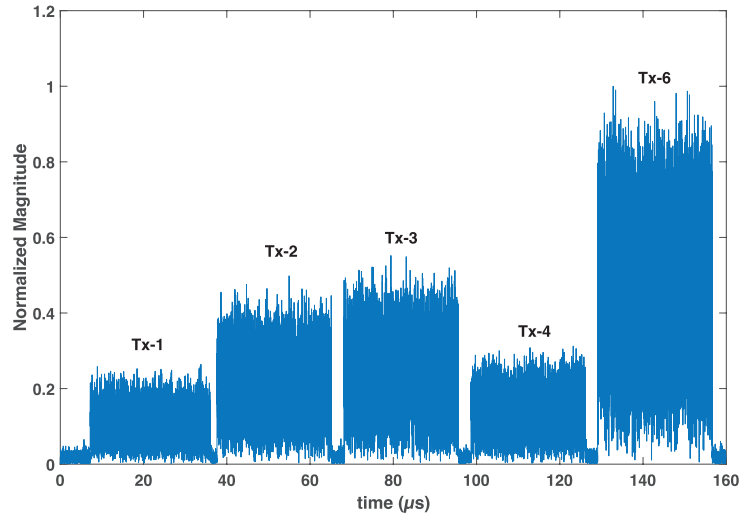
FIGURE 10 Example of a received TDM ranging signal burst from five active transmitters. Tx-5 is deactivated) and the receiver is located at the Reference Point in Figure 16. The SNR values for the signals received from Tx-1 to Tx-4 and Tx-6, were 15.2, 21.7, 22.4, 17.3, and 28.7 dB, respectively.
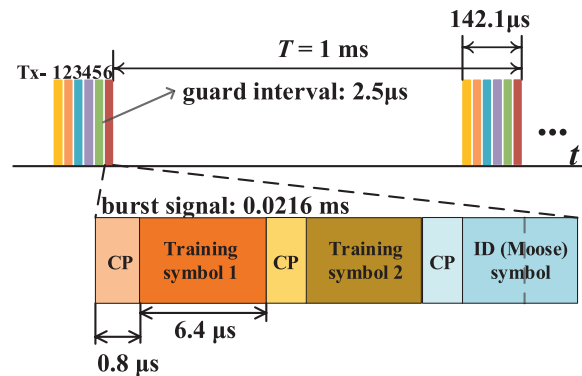

FIGURE 11 A burst-like OFDM signal packet is transmitted by each transmitter Tx-1 to Tx-6, for ranging in a TDM scheme with a period of $T = 1$ ms. Each signal packet contains three training symbols. The first two symbols are for synchronization and channel estimation and the third is for transmitter identification.

the receiver can operate in an asynchronous stand-alone mode in which the ranging bursts are detected in real-time by using a matched-filter technique in the USRP field-programmable gate array (FPGA). If the receiver clock is stable up to 0.1 ppm (10^{-7} s/s); then in a 160 μs time span to allow for the arrival of signals from all Txs, the Rx-clock offset may change by 16 ps, and hence generate a 4.8 mm offset.

4.2.4 | X310 FPGA developments

The X310 USRP transmitters were designed to transmit generic wideband ranging signals as sequences of samples, e.g., representing QPSK modulated PRN or OFDM signals. The ranging signal is constrained to a maximum bandwidth of 160 MHz and a maximum length of 32,000 samples for each transmitter. It should be represented in a 32 bits per sample (16 bits-I and 16 bits-Q) format. Custom hardware description language (HDL) units were developed for the X310 Kintex7

FPGA that permit it to store a ranging signal burst and perform periodic synchronized transmissions (Diouf et al., 2021). A transmitter USRP is operated as follows. First, the ranging signal is downloaded from the host-PC. After completion, the host-PC is disconnected and the USRP will then periodically and accurately autonomously time stream the ranging signal burst. The receiver USRP samples the incoming TDM burst with ranging signals at 200 Msps and forwards the samples to a connected host-PC for storage and post-processing. For a signal that is sampled continuously at 200 Msps with four bytes per sample, a data throughput of 800 MB/s will be required. This is difficult to sustain continuously and reliably, even by a high-performance PC. This problem can be solved by using a low duty cycle ranging signal. A custom HDL unit was developed which implements temporary storage of the received ranging signal burst samples on the USRP followed by their transfer to the host PC at a sustainable data rate (Diouf et al., 2021). Under these conditions, the receiver USRP only captures the samples taken from the 160 μs time window that contains the ranging signals. In the remaining 840 μs, the samples are transferred to the connected host-PC before the start of the next burst. This results in an average data transfer rate to the host-PC of 128 MB/s, which is sustainable by a high-end PC.

4.3 | Signal Processing and Positioning

4.3.1 | Ranging signal

We present results based on a ranging signal implemented by means of OFDM. This is in wide use in various communication systems, including 4G/LTE (Shamaei & Kassas, 2018) and Wi-Fi (Vasisht et al., 2016). An OFDM signal consists of a large number of closely spaced orthogonal sub-carriers arranged in parallel. As described by Dun et al. (2021b), each transmitter transmits a burst-like signal packet for ranging that contains three training symbols as shown in Figure 11. The first two symbols are used (although one symbol would suffice in principle) for packet synchronization and channel estimation, in which a PRN sequence is QPSK-modulated on all available sub-carriers (i.e., the length of the sequence equals the number of sub-carriers used.) The final symbol for which each transmitter uses a unique Gold sequence, is for transmitter identification by the receiver.

A TDM scheme is applied in the prototype system and a burst-like signal packet is repeatedly transmitted, with a period of $T = 1$ ms. Different transmitters occupy different time slots for transmission within this burst. As mentioned earlier, all transmitters should transmit their ranging signals within a brief interval; thus, the receiver frequency offset and receiver position can be assumed fixed during this interval. For example, as shown in Figure 11, all transmitters will transmit their ranging signals (of actually 21.6 μs with a 2.5 μs guard interval) within 142.1 μs. This is slightly less than the maximum signal duration of 160 μs that was set in the prototype system. The rest of the period T was not used. This strict timing will require the transmitters to be synchronized to a time reference using a timing node as discussed in Section 3. If this is not feasible, synchronization can be carried out using wireless time-transfer as shown in Section 4.5.

For the prototype system, the signal bandwidth of 160 MHz at a center frequency of 3.96 GHz is divided into $M = 16$ signal bands; each band has a bandwidth of 10 MHz and $N = 64$ sub-carriers. Thus, a multiband OFDM (MB-OFDM) signal with 16 bands will be created. For the purpose of ranging, it is not necessary to occupy all signal bands. One can use only a few of these signal bands, including the bands at the edges that are sparsely placed in the available spectrum. Under these

conditions, the ranging performance can still benefit from the large *virtual* signal bandwidth (Dun et al., 2021a).

Once the ranging signals (e.g., the training symbols) are received by the receiver and after packet synchronization, Fourier transformation is performed on the received OFDM symbols to recover the original data bits. If the data bits are *a priori* known to the receiver, as is the case with training symbols, one can estimate the channel frequency response by $\underline{H} = \mathcal{F}\{\underline{r}(t)\} / \mathcal{F}\{s(t)\}$. This principle is applicable regardless of the signal modulation, where $\mathcal{F}\{\cdot\}$ denotes the Fourier transform. For more details on modulation/demodulation of OFDM signals, the reader is referred to the work of Y. Li & Stuber (2006). The estimated (sampled) channel frequency response $\underline{H}$ at all sub-carriers included in this process can be used for channel equalization and also for ranging. Given an L-path channel impulse response as shown in Equation (1), the expectation of the sampled channel frequency response is as described by Dun et al. (2021a) and shown in Equation (6):

$$\mathbb{E}\{\underline{H}\} = \mathcal{F}\{h(t)\} = \boldsymbol{A}(\tau)\boldsymbol{x},$$
$$\boldsymbol{A}(\tau) \in \mathbb{C}^{NM \times L}, \quad \boldsymbol{x} \in \mathbb{C}^{L \times 1}, \tag{6}$$

where $\mathbb{E}\{\cdot\}$ denotes the expectation operator, $\mathbb{C}$ denotes the set of complex numbers, and

$$\left[\boldsymbol{A}(\tau)\right]_{p,l} = \exp\left(-j2\pi f_p \tau_l\right), f_p = f_1 + (p-1)f_\Delta,$$
$$x_l = \alpha_l \exp\left(-j2\pi f_c \tau_l\right).$$

where, $[\cdot]_{p,l}$ denotes the element in the p-th row and l-th column of a matrix, with $p = 1, \ldots, NM$ and $l = 1, \ldots, L$. f_p denotes the frequency of the p-th sub-carrier with respect to the lowest sub-carrier frequency f_1 when all consecutive bands are used, i.e. in case of a full band signal (done here just for explanatory ease). f_Δ denotes the sub-carrier spacing which is equal to the inverse of the OFDM symbol duration without cyclic prefix (CP), f_c denotes the central frequency of the ranging signal, and j denotes the imaginary unit. A delay in time domain shows up as a phase rotation in frequency domain. In model (6) we use this information to estimate the time delay.

The variance matrix $\boldsymbol{Q}_H$ is assumed to be a diagonal matrix as described by Kay (1993) and shown in Equation (7):

$$\boldsymbol{Q}_H = N M \sigma_n^2 \boldsymbol{I}_{NM}, \tag{7}$$

where σ_n^2 denotes the variance of white Gaussian noise (WGN) in the time domain with (2) and I_{NM} denotes an $N M$-by-$N M$ identity matrix.

4.3.2 | *Time delay estimation*

Based on the sampled channel frequency response $\boldsymbol{H}$ and assuming a circular-symmetric complex normal distribution of the noise, one can jointly estimate the time delay for both the LoS path and the reflections using the maximum likelihood (ML) principle (Dun et al., 2021a); (Progri et al., 2005). The cost function is calculated as shown in Equation (8):

$$\hat{\boldsymbol{\tau}} = \arg\min_{\boldsymbol{\tau}} \left\| P^\perp_{\boldsymbol{A}(\boldsymbol{\tau})} \boldsymbol{H} \right\|^2_{\boldsymbol{Q}_H^{-1}}, \tag{8}$$

with projectors in Equation (9):

$$P^{\perp}_{A(\tau)} = I_{NM} - P_{A(\tau)}$$

$$P_{A(\tau)} = A(\tau)\left(A^{H}(\tau)Q_{H}^{-1}A(\tau)\right)^{-1}A^{H}(\tau)Q_{H}^{-1},$$

(9)

and $(\cdot)^{H}$ denoting a Hermitian operator.

Rather than estimating L paths, one can simply consider a single path in the time delay estimation model. The cost function, with Equation (7), then turns into Equation (10):

$$\hat{\tau}_{1} = \arg\min_{\tau} \left\|P^{\perp}_{a(\tau)}H\right\|^{2}_{Q_{H}^{-1}} = \arg\max_{\tau} H^{H}P_{a(\tau)}H$$

$$= \arg\max_{\tau} \frac{H^{H}a(\tau)a^{H}(\tau)H}{a^{H}(\tau)a(\tau)}.$$

(10)

This reduces the computational complexity compared to using the cost function described in Equation (8). This can lead to a better ranging precision (Dun et al., 2021a). Because only a single path is considered in the model for time delay estimation shown in Equation (10), the resulting estimator $\hat{\tau}_{1}$ will be biased in a multipath channel. Using a wideband ranging signal, however, increases the time delay resolution and the bias will be limited. Figure 12 shows the envelope of the multipath error (i.e., the time delay bias using Equation (10) in a two-path channel, hence LoS and a single reflection) as a function of the relative distance $c(\tau_{2} - \tau_{1})$, with the assumption of infinite signal bandwidth, i.e., no filtering applied, and the relative gain (α_{2}/α_{1}) set to 0.6, similar to analyses described in Braasch (2017). Three types of ranging signals are considered in Figure 12, including two adjacent OFDM signals of 64 sub-carriers (each spanning a band of 10 MHz), in total spanning a 20 MHz band, 16 adjacent OFDM signals spanning a 160 MHz band, and the GPS L5 signal with a chip rate of 10.23 Mcps using a 0.5 chip-spaced correlator. Figure 12 demonstrates that a large signal bandwidth for ranging improves the separation of multipath reflections and effectively mitigates the multipath error. Using 160 MHz of bandwidth for ranging,
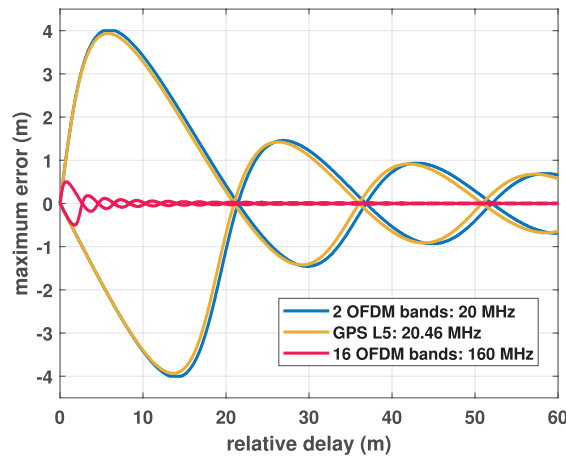

FIGURE 12 Multipath error envelopes for three unfiltered, infinite-bandwidth signals. Shown are the signals from two adjacent OFDM bands (20 MHz), a signal from 16 adjacent OFDM bands (160 MHz), and GPS L5 signal (10.23 Mcps) in a single reflected path scenario with the relative path gain α_{2}/α_{1} set at 0.6.

the resulting maximum multipath error is about 0.5 m. This is much smaller than the multipath error of approximately 4.0 m that one would obtain using a bandwidth of 20 MHz.

4.3.3 | *Positioning model*

Based on the time delay estimate $\hat{\tau}_r^i$ from Equation (10), and dropping the index '1', the associated pseudo-range measurement obtained at time instant t is given in Equation (11) by

$$\underline{\rho}_r^i(t) = c\hat{\underline{\tau}}_r^i(t) = d_r^i(t) + c\tau_h + c\delta_r(t) + \underline{e}_r^i,$$

(11)

where d_r^i denotes the geometric propagation distance between the i-th transmitter (Tx) and the receiver r (Rx), c denotes the speed of light, τ_h denotes the hardware delay of the Tx-Rx link (e.g., introduced by the RF-front end), $\delta_r(t)$ denotes the receiver clock offset (the receiver is generally not synchronized to the transmitters), and e_r^i is the measurement error. Note that the update period of the pseudo-range measurement is equal to the transmission period of the signal packet T (see Figure 11). All radio transmitters in the prototype system are synchronized by the optically-distributed time and frequency reference signal (i.e., 1 PPS and 10 MHz, respectively); the receiver runs on its own clock. Hence, the clock offset $\delta_r(t)$ in Equation (11) is a receiver-dependent parameter and is the same for all Tx-Rx links. Because the same type of hardware is used for all transmitters, the hardware delay τ_h is assumed to be a receiver-dependent parameter (with the transmitter contributions to the hardware delay included). If there is a transmitter-dependent offset (e.g., introduced by different hardware delays across transmitters) which was not considered in the measurement model, it will be included in the error $\underline{e}_r^i$ and the resulting position solution will be biased.

With the positioning model below, the hardware delay τ_h cannot be estimated separately from the receiver clock offset $\delta_r(t)$. This means that, in the sequel, the clock offset will include the hardware delay and their combined effects will be estimated.

The unknown receiver position $\boldsymbol{x}_r$ (i.e., x_r, y_r, z_r) is involved non-linearly in the propagation distance $d_r^i(t)$ as described in Equation (12):

$$d_r^i(t) = \sqrt{\left(x_r(t) - x^i\right)^2 + \left(y_r(t) - y^i\right)^2 + \left(z_r(t) - z^i\right)^2},$$

(12)

where (x^i, y^i, z^i) denotes the position of the i-th transmitter. The propagation distance $d_r^i(t)$ can be linearized at the approximated receiver position $\boldsymbol{x}_r^{(0)}$ as indicated in Equation (13):

$$d_r^i(t) \approx d_r^i(t)|_{\boldsymbol{x}_r^{(0)}} + \underbrace{\partial_{\boldsymbol{x}_r^{\mathrm{T}}} d_r^i(t)|_{\boldsymbol{x}_r^{(0)}}}_{\boldsymbol{g}_r^i(t)^{\mathrm{T}}} \underbrace{\left(\boldsymbol{x}_r(t) - \boldsymbol{x}_r^{(0)}(t)\right)}_{\Delta\boldsymbol{x}_r(t)},$$

(13)

where $(\cdot)^{\mathrm{T}}$ denotes transposition.

The receiver position solution can then be estimated iteratively using the Gauss-Newton method. The initial value of the approximation of the receiver position can be derived by a direct method which provides a closed-form solution with no iteration (Yan et al., 2010). Assuming that K transmitters are used, and the non-linear propagation distance is linearized by Equation (13) then the

time-delay based positioning model, omitting the measurement error, is given by Equation (14):

$$\Delta\boldsymbol{\rho}_r = \begin{bmatrix} \Delta\rho_r^i(t) \\ \vdots \\ \Delta\rho_r^K(t) \end{bmatrix} = \begin{bmatrix} \mathbf{g}_r^1(t)^\mathrm{T} & 1 \\ \vdots & \vdots \\ \mathbf{g}_r^K(t)^\mathrm{T} & 1 \end{bmatrix} \begin{bmatrix} \Delta\boldsymbol{x}_r(t) \\ \delta_r(t) \end{bmatrix}, \tag{14}$$

where

$$\Delta\rho_r^i(t) = \rho_r^i(t) - d_r^i(t)|_{\boldsymbol{x}_r^{(0)}}.$$

The receiver position coordinates and the clock offset can be estimated according to the ML principle when the pseudo-range observables are normally distributed within the variance matrix $\boldsymbol{Q}_\rho$ as shown in Equation (15):

$$\left[\boldsymbol{Q}_\rho\right]_{i,i} = c^2\sigma_{\hat{\tau}_r^i}^2 = \sigma_{\rho_r^i}^2. \tag{15}$$

where $\sigma_{\hat{\tau}_r^i}^2$ depends on the frequency bands used and the SNR (through σ_n^2 and α_1^2) as described in Equation(3).

4.4 | Ground-Truth Trajectory

The TNPS-receiver (Rx) and its antenna were attached to a simple trolley as shown in Figure 13 to facilitate both static and slow kinematic measurements. To determine the ground-truth position of the receiver in both modes, two 360-degrees prisms were also attached to the trolley; each was tracked by a robotized land-surveying total station. The total station measures vertical and horizontal angles and slant distance. In this short range set-up (maximum 40 m), the distance measurement determines the resulting positioning precision of the prism, which is typically at the several millimeter level. During the experiments, the receiver on the trolley moved on a flat level road. Therefore, horizontal two-dimensional ground-truth positions are determined. The heights of the receiver antenna and the two prisms were determined *a priori*, and they are assumed to remain constant during the experiment.

The total station provides measurements with an update rate between 1–10 Hz, depending on the speed of the receiver. The TNPS provides receiver position solutions with an update rate of 1 kHz, which is much higher than the measurements obtained from the total stations. Hence, to construct the ground-truth of the receiver
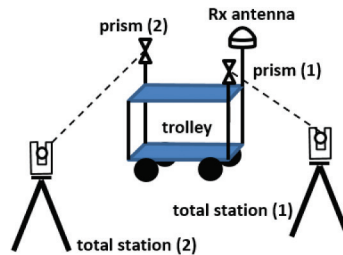

FIGURE 13 Set up of the receiver (Rx) antenna and determination of its ground-truth trajectory. The receiver antenna and two 360-degrees prisms were attached to a trolley and the two prisms were tracked separately by two total stations.
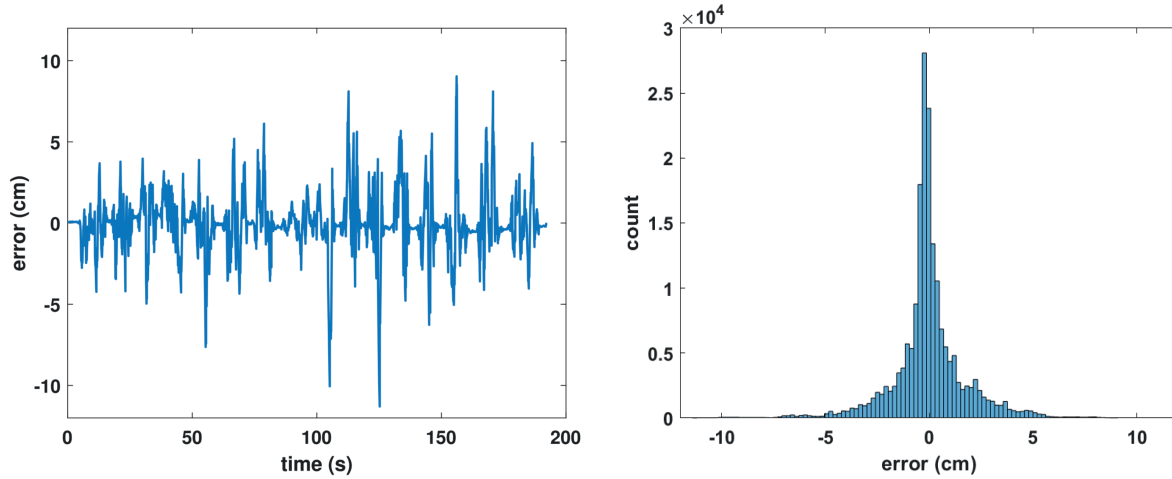
FIGURE 14 Difference in distance between two prisms based on reconstructed trajectories and *a priori* measured distance. This is presented as a function of measurement time (at the left) and in a histogram (at the right). The position update rate was 1000 Hz.

trajectory, the positions determined by the total stations need to be interpolated. A piece-wise linear least-squares interpolation was done for both coordinates with a moving window of five positions. In this case, the receiver is assumed to be moving along a straight line with constant velocity in this time window. Eventually, the positions of the prisms are interpolated with an update rate of 1 kHz based on the estimated linear model. The two total stations are not synchronized. The time lag between the two can be retrieved by shifting one of the time series trajectories until the motion patterns of the two trajectories are optimally matched.

The coordinates determined by the total stations are expressed in a local reference system with the origin at "total station (1)" shown in Figure 13. These are then rotated into a local east-north-up (ENU) reference system, after determining the azimuth with two GPS receivers on the baseline formed by the two total stations. Next, with the distances between the prisms and the Rx antenna on the trolley that were determined *a priori*, the ground-truth trajectory of the Rx antenna can be reconstructed. Finally, to compute the position error in the experiment, the trajectory determined by the TNPS and the ground-truth should also be optimally matched, as the receiver is not synchronized with the total stations.

To evaluate the quality of the reconstructed ground-truth trajectories, one can retrieve the horizontal distance between the two prisms based on their aligned trajectories and compare it to the (fixed) horizontal distance between the two prisms, as determined before the experiment. This is shown in Figure 14 for one of the runs. The RMSE of the resulting difference is 1.8 cm. Hence, one can assume that the error in the reconstructed ground-truth receiver position is at the cm-level and that most of the uncertainty is likely introduced by the interpolation. This is because the motion of the trolley was neither on a straight line nor at a constant velocity all the time. Additional error may be introduced by small changes in height, because the road was not perfectly flat and level.

The total stations have also been used to determine the positions of all transmitter antennas. They are in the same local ENU system as was used for the receiver ground-truth trajectory. The phase center offset of the antennas, which was 4.5 cm in height with respect to the antenna ground plane as determined *a priori* in the lab, has been taken into account.

4.5 | TNPS-Prototype Results

In this section, we provide results obtained with the TNPS prototype deployed at The Green Village in mid-September 2020. Several experiments were carried out in both static and kinematic modes, the latter with a trolley and a car.

The position results are by default based on time delay measurements as outlined in Section 4.3. Time delay estimation was done on a per packet basis and the position-time solutions were obtained correspondingly at a rate of 1000 Hz using the model shown in Equation (14). These position-time solutions are known as snapshot solutions and are obtained instantaneously, hence no time averaging or Kalman filtering have been applied. Obtained position solutions are compared to the ground truth trajectory discussed in Section 4.4. The resulting position errors are presented.

We have restricted positioning with the prototype-system to two dimensions. The receiver antenna is placed at a 1.5 to 2 m height and the transmitter antennas are all at a 3.5 to 5.5 m height. Thus, there is minimal diversity in height and the elevation angles are all fairly small. The receiver antennas on the trolley and on the car were at 1.573 m at 2.006 m in height, respectively. These heights are assumed constant and have been substituted in Equation (13) to allow for two-dimensional positioning using the prototype system.

Results of a kinematic run with the trolley are presented when the receiver was also connected to an active WR timing node. Time delay estimation and positioning were performed without this information, hence using the model in Equation (14) and estimating a receiver clock offset every epoch. Finally, we also present results of a kinematic run with a car with the receiver running in a fully asynchronous mode.

Based on the model shown in Equation (14) for estimating a two-dimensional position and a receiver clock offset, and assuming the variance matrix shown in Equation (15) to be an identity matrix (based on a standard deviation of $\sigma_\rho = 3$ cm), the precision of the two-dimensional position is shown as $\sqrt{\sigma_{\text{East}}^2 + \sigma_{\text{North}}^2}$ in Figure 15 for the area of the experiment. This quantity is known as the horizontal
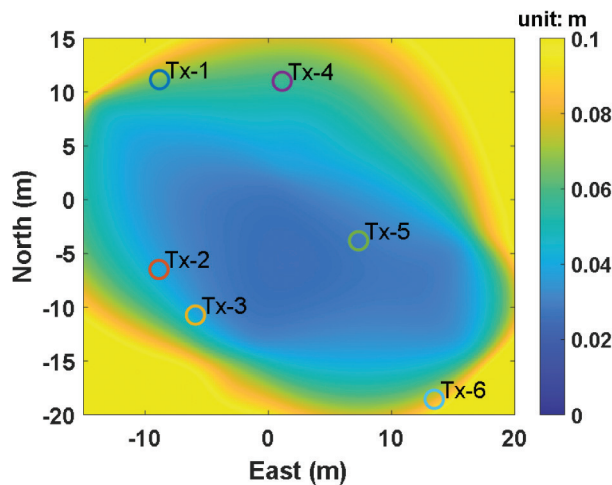

FIGURE 15 Precision of horizontal positioning. This is shown by means of the horizontal dilution of precision (HDOP) scaled with the unit measurement standard deviation ($\sigma_\rho = 3$ cm), hence $\sqrt{\sigma_{\text{East}}^2 + \sigma_{\text{North}}^2}$ in m. The values at the edges of the graph have intentionally been clipped and set to 0.1 m, in order to include the details shown in the coverage area.
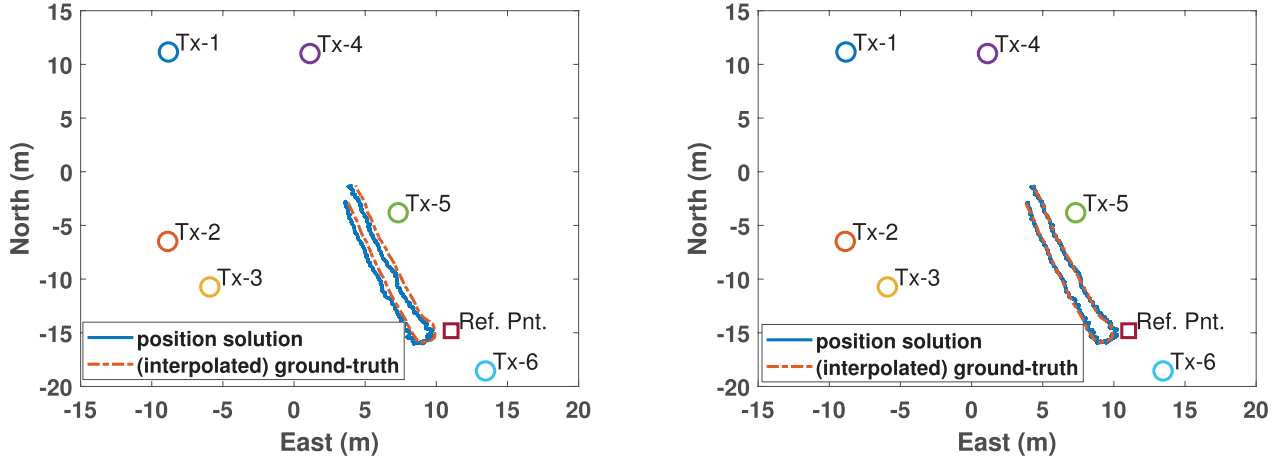
FIGURE 16 The geometry of the six transmitters Tx-1 to Tx-6 with a 3.5 minute trolley run with a positioning update frequency of 1000 Hz. The reference point (Ref. Pnt.) indicates the measurement location of the results in Figure 10, and position solution both with (right) and without correction (left).

dilution of precision (HDOP) (Teunissen & Montenbruck, 2017), although we included here the measurement variance σ_ρ^2 rather than presenting just the geometric factor. Clearly, the positioning geometry is good in the area enclosed by the transmitters. Also the track of the receiver in the kinematic experiment is within this area.

Figure 16 documents the horizontal positioning results of one of the runs with the trolley. In this case, the trolley moved forward on the local road, made a U-turn, went back, and eventually terminated at a point close to where it started. In total, the trolley moved by about 30 m. It occasionally made some stops on the way, and the run lasted 3.5 minutes. The TNPS-position solutions are shown in blue based on time delay measurements. The corresponding ground-truth is shown as a red dashed line. The graph at left shows the results directly from the measurements. For the graph at right, compensation was introduced to adjust for systematic (constant) biases in the measured pseudoranges of transmitters Tx-5 and Tx-6. After compensation the track is spot-on, and deviations are only at the 1–2 decimeter level.

Figure 17 presents the estimated receiver clock offset $\delta_r(t)$ as indicated in Equation (14). In this trolley run, the receiver was connected to an active WR timing node. Ideally, this should result in a zero clock offset. The estimated clock offset appears constant and the systematic offset of about 17 μs is caused by transmitter and receiver front end delays τ_h. The empirical standard deviation is only 4 cm, i.e., 0.1 ns in terms of time delay. These results show the high-precision wireless time-transfer potential of this system.

Figure 18 shows the horizontal position error as a function of time, at left for a run with the trolley (the same run as with Figure 16), and at right for a run with a car, in which the receiver was not connected to a WR timing node, and hence running in a true asynchronous mode. We note that this latter run lasted 71 seconds. Table 2 presents the statistics of both runs in terms of mean position error, empirical standard deviation, and RMSE in meters, expressed in local east and north, for a run with the trolley and the car. The RMS position error comes close to a one decimeter in both cases.

Building on the suggestion given in Section 4.3 the data of the run shown in Figure 16, with empirical statistical values given in Table 2, have been
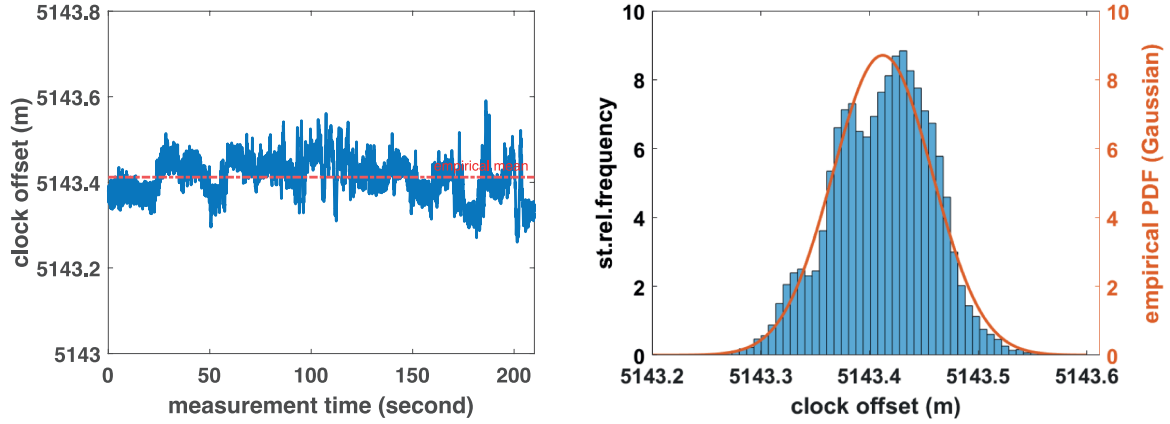
FIGURE 17 Estimated receiver clock offset with wireless time transfer where the receiver is operated in synchronous mode, but was processed as if in asynchronous mode. Shown is $c\delta_r(t)$, Equation (11), with the offset $c\tau_h$ included. The empirical mean, for the most part caused by hardware delays τ_h, is 5143.41 m and the empirical standard deviation is 0.04 m.
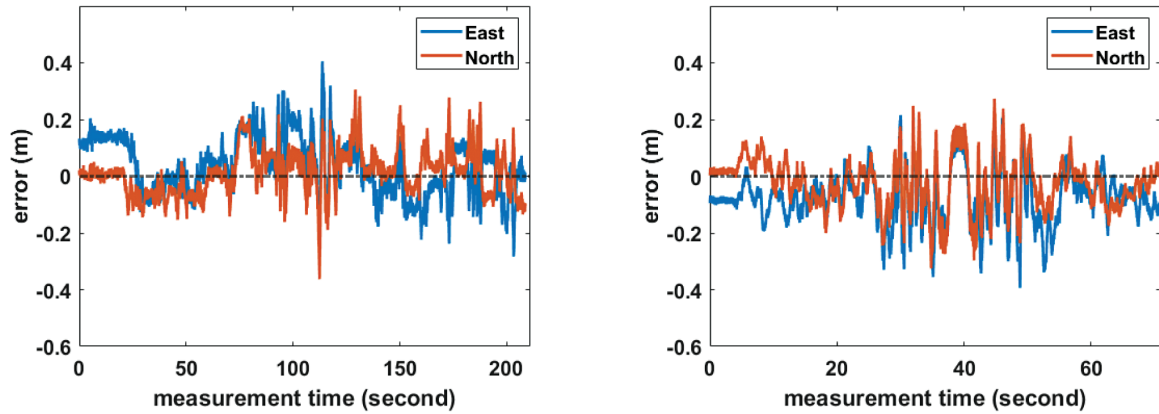

FIGURE 18 Positioning error of the receiver (Rx) trajectory for the trolley (synchronous, at left) and the car (asynchronous, at right). In both cases the asynchronous positioning model in Equation (14) was used with position coordinates and clock offset.

TABLE 2
Statistics for Figure 18, Including Empirical Mean, Standard Deviation and RMSE of Position Error in East and North Based on Time Delay Measurements and Using 160 MHz of Bandwidth.

Position error	unit: cm	mean	std.	RMSE
Sync. setup	**East**	2.38	9.65	9.94
	North	1.23	7.56	7.65
Asyn. setup	**East**	−7.75	9.06	11.92
	North	−2.63	9.01	9.39

reprocessed. Only a few bands were used and effectively a frequency-sparse signal was employed (Dun et al., 2021a), rather than the full 160 MHz band. Muting 9 of 16 bands and using only the 7 that remained of 10 MHz each, including the bands at the edges (here, bands 1, 2, 5, 6, 12, 13 and 16) resulted in very similar time-delay based positioning results when the main-lobe of the cost function was correctly identified. We observed no noticeable degradation of performance nor any issues with bias or spread.
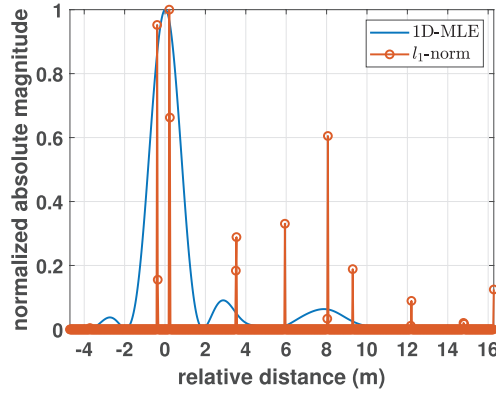
FIGURE 19 Estimated channel impulse response by using 1D maximum likelihood estimator (MLE) as per Equation (10) and sparsity-promoting l_1-norm with a redundant basis generated by delays at a resolution of 0.1 ns.

Figure 19 documents an example of a CIR obtained in the experiment, specifically of the signal received from transmitter Tx-2. After packet synchronization of the received signal and fast Fourier transformation (FFT), the channel frequency response as indicated in Equation (6) was obtained using a known training symbol. For the blue line, labeled 1D MLE, we consider only a single path, $L = 1$, and show the cost function from Equation (10), as a function of time delay τ (expressed in meters). This is equivalent to using a single arm cross-correlator receiver. The red stems show the channel response using the joint estimation of time delay and gain with a model as shown in Equation (6) (Dun et al., 2020); (Berger et al., 2010). An entire range (dictionary) of delays was put forward with a resolution of 0.1 ns, although at the same time a penalty is introduced in the form of a minimum norm on vector x as the solution to Equation (6). This channel response estimate is labeled l_1-norm, and the solution is forced to be sparse. It is clear that multiple signal reflections were received, including several that were comparatively strong and close to the LoS path. This was likely caused by the objects directly adjacent to the road, including brick-wall houses, as shown in Figure 8. According to Figure 12, a fairly strong reflection can induce a multipath error in time delay range of only up to 0.5 m when using the full 160 MHz of bandwidth. This was confirmed empirically by the positioning errors that incidentally reached 0.3–0.4 m at most as shown in Figure 18, based on six transmitters, and noting an HDOP of approximately 1 along the trajectory covered in Figure 15.

As a final experimental verification of the effectiveness of a large bandwidth for ranging to mitigate the impact of multipath, the data of the run performed with the trolley in Figure 18 at left were reprocessed using only 20 MHz of bandwidth (2 adjacent OFDM bands of 10 MHz each) rather than the full 160 MHz, as shown in Figure 20. The range of the vertical axis is now larger by a factor of 10 (compared to Figure 18). As shown by the blue curve in Figure 12, multipath errors can then be as high as several meters. With 20 MHz of bandwidth, the RMSE of the position error in east and north are 82.06 cm and 68.21 cm, respectively, and can be compared with values shown in Table 2.

Figure 21 also demonstrates the potential of the system to deliver high-precision positioning results by means of measurements of the carrier phase of the burst signal. The carrier phase is determined by phase rotation of the estimated (complex) gain of the first path, shown as x_1 in Equation (6). Carrier phase measurements are inherently ambiguous, and, because of initial phase offsets in both
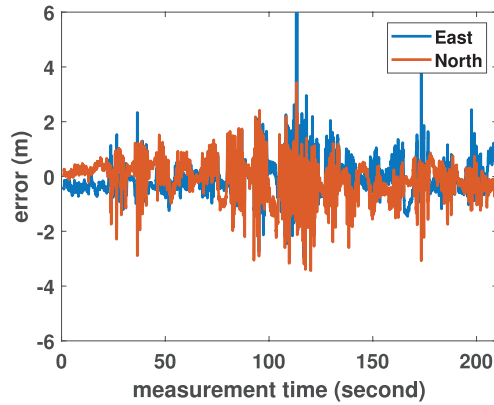
FIGURE 20 Positioning error of the receiver (Rx) trajectory for the trolley, based on time delay measurements, using only 20 MHz of bandwidth instead of the full 160 MHz. These findings can be compared to those in Figure 18 (at left). The position error RMSE in east and north are 82.06 and 68.21 cm, respectively.
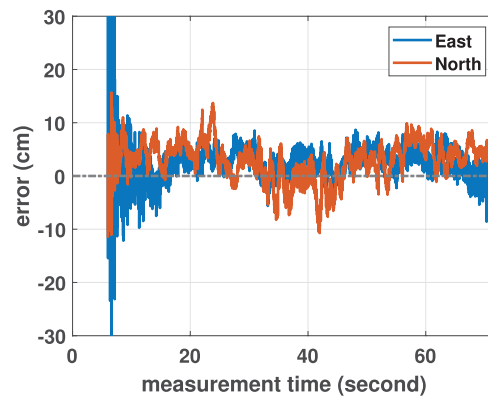

FIGURE 21 Positioning error for two-epoch, carrier-phase-only float position solution estimation with empirical means of 2.5 cm (east) and 2.9 cm (north), empirical standard deviations of 3.4 cm (east) 3.6 cm (north), and empirical RMSEs of 4.2 cm (east), 4.6 cm (north).

transmitter and receiver, the ambiguity does not initially emerge as an integer. The results shown in Figure 21 pertain to float solutions, based on unwrapped carrier phase measurements, with the remaining initial carrier phase cycle ambiguities estimated as constant real-values. As we present here a carrier-phase-only solution, at least two epochs of measurements are needed accompanied by a change of geometry. The first epoch is fixed and the second epoch varies across the duration of the 71 second run. Only two epochs of measurements are used for each solution shown. The solution is shown as a function of the second epoch, and only starts after five seconds to provide time for the necessary change in geometry. In this run, the receiver was installed on a car and operated in asynchronous mode. The carrier phase measurement model and additional results are presented in Dun et al. (2021b).

The results shown in Figure 16 (at left) indicate a systematic bias in the estimated positions. Investigations in the laboratory revealed that the transmission times of the RF signals, particularly those from Tx-5 and Tx-6, show a delay of about 1.5 ns with a standard deviation of 180 ps compared to the other transmitters. Additional measurements revealed that the 1 PPS of the WR timing nodes were well aligned with a maximum deviation of 100 ps, but that the 10 MHz signals of the timing
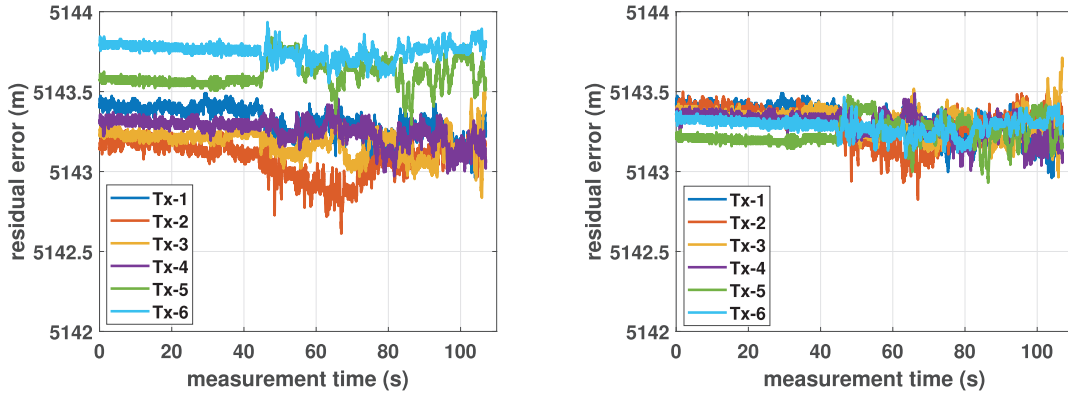
FIGURE 22 Difference between the measured time delay and the ground-truth propagation time delay without correction (left) and with *a posteriori* correction (right) of the transmitter timing offsets. In this run, the receiver was static during the first 45 seconds.

nodes were not well aligned to the 1 PPS signals and had different offsets of up to 600 ps (although repeatable with a standard deviation < 40 ps). These phase offsets of the 10 MHz should have been calibrated. By contrast, all USRP were connected to the 1 PPS and 10 MHz signals of a National Instruments CDA-2990 clock distributor, with deviations of 60 ps and 20 ps, respectively. The offsets in the measured RF transmission delays were on the order of 100 ps with a standard deviation of 25 ps. Based on these observations, the 10 MHz offsets are suspected to be the cause of the systematic offsets of about 1.5 ns in the measured ranges, most notably present in the pseudoranges of Tx-5 and Tx-6. These offsets are shown in Figure 22 (at left). The RF transmission delays have been determined *a posteriori* and were used to correct the timing offsets. The corresponding positioning results are shown in Figure 16 (at right).

Figure 22 shows the residual range error for each transmitter without (at left) and with a-posteriori correction (at right). The receiver was synchronized, so the clock offset $\delta_r(t)$ as shown in Equation (11) should be a constant. Hardware delays τ_h are considered together with the receiver clock offset provided that they originate from the receiver, or, if they originate from the transmitter, they are identical across all transmitters. With given transmitter positions and using the known ground-truth position of the receiver, the distance d calculated in Equation (11) is known. As shown in Figure 22 in blue, red, yellow and purple, the residual pseudorange error for Tx-1 to Tx-4, which are fairly constant and at the same level, represent the clock offset. The residual error of the pseudorange from Tx-5 and Tx-6 (in green and light-blue) compared with Tx-1 to Tx-4, show a clear offset of about 1.5 and 1.9 ns, respectively. After correction, all residual errors are at the same constant level.

5 | DISCUSSION AND OUTLOOK

The results presented in this paper demonstrate the technical feasibility of a terrestrial-networked positioning system (TNPS) which could provide a backup for GPS/GNSS PNT services and also be used to improve PNT performance. However, its viability as a general GPS/GNSS complement or back-up system depends critically on its scalability and ease of implementation on a larger metropolitan, regional, or even national scale. Here we identify three major challenges

for implementation. We propose solutions for each of these challenges based on the technology demonstrated here. Because the architecture of our hybrid optical-wireless terrestrial PNT system resembles that of a mobile telecommunication network, the solutions can be adapted to implementation using the existing mobile telecommunication infrastructure, although other approaches are conceivable as well.

The first, and arguably largest challenge towards large-scale implementation is the scarcity of radio spectrum. This prevents large-scale (U)WB signal transmissions for PNT. Previously, it has been shown that the benefits of wideband ranging can also be realized by use of narrow (~ 10 MHz) bands that are sparsely placed across the spectrum to create a large virtual bandwidth (Dun et al., 2019). A multiband signal creates a type of diversity gain against deep fades due to multipath propagation. In other words, it becomes much less likely to find all bands simultaneously in a deep fade. Interestingly, the radio spectrum currently licensed to mobile telecommunication providers corresponds to this sparse band configuration, with each provider having access to multiple 5–15 MHz bands in the frequency range 600–3500 MHz. The spectrum required for sparse-band (U)WB transmission is therefore already available to potential providers of terrestrial PNT signals.

The second challenge is the scarcity of capacity within the licensed narrow bands, and the compatibility of PNT signals with the signal modulation formats used in 4G and 5G radio access networks (RANs). We have shown here that accurate ranging is feasible with a duty cycle of 0.1, thus, 90% of the band capacity remains available for telecommunications. In this demonstration we did not investigate nor did we run into any limits regarding duty cycle, however, the overhead for PNT transmissions in 4G mobile networks may be as large as 3.75% (Fischer, 2014). Furthermore, we have demonstrated positioning through OFDM modulation, which is similar to the modulation format used in 4G and 5G RANs. This suggests that radio signals for decimeter positioning may be generated using the hardware of mobile base stations with minimal changes and an acceptable loss of capacity provided that the base station is time-synchronized with other base stations to within a few 0.1 ns.

The third challenge is to transport sub-nanosecond time from a common reference time scale to the transmitters of the terrestrial radio PNT system covering distances of more than 100 km. Again, existing (mobile) telecommunication infrastructure may provide a solution. We can use the fixed-network architecture of mobile networks as an example. A reference time scale (for example a UTC realization at a National Metrology Institute or National Time Laboratory) could synchronize a WR network having a point of presence in one of the central offices of the core network of a mobile network operator. Core networks make use of high-capacity dense wavelength division multiplexing (DWDM) systems. Earlier work has shown that WR can coexist with such systems with the WR optical signals propagating side-by-side with the many DWDM optical signals that carry live production data traffic over the same optical fiber (Boven et al., 2019). The Gigabit Ethernet connectivity offered by WR makes this suitable for control-plane communication through optical supervisory channels already present in DWDM systems (Nuijts & Koelemeij, 2016). Sub-nanosecond time distribution may therefore be implemented in core and metro-core optical networks without compromising the performance of the DWDM system used. At sites where the (metro) core network branches into aggregation and backhaul network layers that eventually connect to the radio base stations, WR wavelengths may be wavelength-division multiplexed with the wavelengths used in these layers and transported to PNT base stations

over existing optical fibers. In some segments of the network, use may be made of free-space millimeter-wave (mm-wave) connections instead of optical fiber. WR has been shown to be also compatible with mm-wave communication links (Gilligan et al., 2020).

As noted above, WR requires bidirectional transmission of optical signals through the same optical fiber if sub-nanosecond performance is to be achieved. Existing optical networks, however, are typically designed to use fiber pairs with upstream optical data traveling in one direction through one fiber and downstream data traveling through the other. In such systems, a bidirectional wavelength channel for WR can nevertheless be achieved using WDM methods as these may also include dedicated bidirectional optical amplifiers for the WR optical signals (Lopez et al., 2010); (Dierikx et al., 2016); (Dierikx et al., 2019); (Smets, 2016); (Boven et al., 2019).

The implementation of timing and positioning features as described above would represent significant evolution of the mobile network infrastructure as it will extend its role from a telecommunications-only resource to telecommunications and timing and positioning that would be independent of, and beyond that provided by, GPS/ GNSS. This type of system may mitigate the risks associated with the over-reliance on GPS/GNSS and may lead to numerous new applications facilitated by the combination of high-throughput connectivity and precise time and position information. Important examples include autonomous driving, advanced mobile telecommunication features (H. Li et al., 2017), time stamping of financial and other data, and sustainable energy grids (Sadlier et al., 2017); (Muljadi et al., 2014).

6 | CONCLUSIONS AND SUMMARY

In this paper, we present a terrestrial optical-wireless system that offers decimeter-level positioning in an urban environment. It does so by relying on an optically-distributed atomic time reference and using wideband radio signals to combat multipath. A working prototype of this system was successfully deployed in a relevant outdoor scenario.

Fiber-optic connections can carry optical time synchronization signals over tens of kilometers, and much further with regeneration and amplification. These signals can be transmitted together with ordinary data traffic on a fiber. By using wideband radio signals, high accuracy ranging by means of signal time delay measurements can be achieved in multipath radio environments such as those typically found in built-up urban areas.

The scalability of the system and its compatibility with existing telecommunication systems highlight the potential of this terrestrial optical-wireless system as a wide-area PNT complement to GNSS.

REFERENCES

Barnes, J., Rizos, C., Kanli, M., Pahwa, A., Small, D., Voigt, G., Gambale, N., & Lamance, J. (2005). High accuracy positioning using Locata's next generation technology. *Proc. of the 18th International Technical Meeting of the Satellite Division of the Institute of Navigation (ION GPS/GNSS 2005),* Long Beach, CA. 2049–2056.

Barnes, J., Rizos, C., Wang, J., Small, D., Voigt, G., & Gambale, N. (2003). Locata: A new positioning technology for high precision indoor and outdoor positioning. *Proc. of the 16th International Technical Meeting of the Satellite Division of the Institute of Navigation (ION GPS/GNSS 2003),* Portland, OR. 1119–1128.

Beeldmateriaal Nederland. (2021). *Aerial photograph of TU Delft campus.* Amersfoort, The Netherlands. https://www.beeldmateriaal.nl/

Berger, C. R., Wang, Z., Huang, J., & Zhou, S. (2010). Application of compressive sensing to sparse channel estimation. *IEEE Communications Magazine, 48*(11), 164–174. https://doi.org/10.1109/MCOM.2010.5621984

Bergeron, H., Sinclair, L. C., Swann, W. C., Khader, I., Cossel, K. C., Cermak, M., Deschênes, J., & Newbury, N. R. (2019). Femtosecond time synchronization of optical clocks off of a flying quadcopter. *Nature Communications, 10*(1)*, 1–7.* https://doi.org/10.1038/s41467-019-09768-9

Bigler, T., Treytl, A., Löschenbrand, D., & Zemen, T. (2018). High accuracy synchronization for distributed massive MIMO using white rabbit. *Proc. of the IEEE International Symposium on Precision Clock Synchronisation for Measurement Control, and Communication (ISPCS 2018*), Geneva, Switzerland. https://doi.org/10.1109/ISPCS.2018.8543079

Boven, P., van Tour, C., & Smets, R. (2019). *Demonstration of VLBI synchronization via existing SURFnet/LOFAR network.* ASTERICS-H2020-653477 – Report D5.14. https://www.asterics2020.eu/sites/default/files/documents/asterics-d5.14.pdf

Braasch, M. (2017). Chapter 15 on Multipath. *Springer Handbook of Global Navigation Satellite Systems*, 443–468. https://ge0mlib.com/papers/Books/nav03_Handbook_of_Global_Navigation_Satellite_Systems.pdf

Daniluk, G. (2015). White Rabbit calibration procedure, version 1.1 (No. CERN BE-CO-HT). https://www.ohwr.org/documents/213

Decawave. (2020). http://www.decawave.com/. [online, accessed June 2022]

Defraigne, P. (2017). Chapter 41 on GNSS time and frequency transfer. *Springer Handbook of Global Navigation Satellite Systems,* 1187–1206. https://ge0mlib.com/papers/Books/nav03_Handbook_of_Global_Navigation_Satellite_Systems.pdf

Dierikx, E., Wallin, A., Fordell, T., Myyry, J., Koponen, P., Merimaa, M., Pinkert, T., Koelemeij, J., Peek, H., & Smets, R. (2016). White Rabbit precision time protocol on long distance fiber links. *IEEE Transactions on Ultrasonics, Ferroelectrics, and Frequency Control*, *63*(7). https://doi.org/10.1109/TUFFC.2016.2518122

Dierikx, E., Xie, Y., van Veghel, M., Waller, P., Valceschini, R., Weber, J., Plantinga, A., Burger, B., Koelemeij, J., van Tour, C., Savencu, A., Coutereel, F., & Pirée, H. (2019). Optical fiber trans-national time transfer for comparing two UTC realisations. *Proc. of the Joint Conference of the IEEE International Frequency Control Symposium and European Frequency and Time Forum (EFTF/IFC 2019),* Orlando, FL. 1–2. https://doi.org/10.1109/FCS.2019.8856091

Diouf, C., Dun, H., Janssen, G., Dierikx, E., Koelemeij, J., & Tiberius, C. (2022). A terrestrial networked positioning system - better performance combing fiber optics and wideband radio. *GPS World - Innovation Column*, *33*(5), 44–49. https://editions.mydigitalpublication.com/publication/?i=746327

Diouf, C., Dun, H., Kazaz, T., Janssen, G., & Tiberius, C. (2020). Demonstration of a decimeter-level accurate hybrid optical wireless terrestrial positioning system. *Proc. of the 33rd International Technical Meeting of the Satellite Division of the Institute of Navigation (ION GNSS+ 2020),* St. Louis, MO. 2220–2228. https://doi.org/10.33012/2020.17528

Diouf, C., Janssen, G. J. M., Dun, H., Kazaz, T., & Tiberius, C. C. J. M. (2021). A USRP-based testbed for wideband ranging and positioning signal acquisition. *IEEE Transactions on Instrumentation and Measurement*, *70*, 1–15. https://doi.org/10.1109/TIM.2021.3065449

Dun, H., Tiberius, C. C. J. M., Diouf, C., & Janssen, G. J. M. (2020). Sparse signal bands selection for precise time-based ranging in terrestrial positioning. *Proc. of the IEEE/ION Position, Location and Navigation Symposium (IEEE/ION PLANS 2020)*, Portland, OR. 1372–1380. https://doi.org/10.1109/PLANS46316.2020.9110197

Dun, H., Tiberius, C. C. J. M., Diouf, C. E. V., & Janssen, G. J. M. (2021a). Design of sparse multiband signal for precise positioning with joint low-complexity time delay and carrier phase estimation. *IEEE Transactions on Vehicular Technology*, *70*(4), 3552–3567. https://doi.org/10.1109/TVT.2021.3066136

Dun, H., Tiberius, C. C. J. M., Diouf, C., & Janssen, G. J. M. (2021b). Terrestrial precise positioning system using carrier phase from burst signals and optically distributed time and frequency reference. *Proc. of the International Technical Meeting of the Institute of Navigation (ITM 2021)* San Diego, CA. 510–524. https://doi.org/10.33012/2021.17846

Dun, H., Tiberius, C. C. J. M., Janssen, G. J. M., & Diouf, C. (2019). Time delay estimation based on multi-band multi-carrier signal in multipath environments. *Proc. of the 32nd International Technical Meeting of the Satellite Division of the Institute of Navigation (ION GNSS+ 2019),* Miami, FL. 2299–2313. https://doi.org/10.33012/2019.16958

Fischer, S. (2014). *Qualcomm technical note: Observed time difference of arrival (OTDOA) positioning in 3GPP LTE* (Tech. Rep.). Qualcomm. https://www.qualcomm.com/media/documents/files/otdoa-positioning-in-3gpp-lte.pdf

Gilligan, J. E., Konitzer, E. M., Siman-Tov, E., Zobel, J. W., & Adles, E. J. (2020). White Rabbit time and frequency transfer over wireless millimeter-wave carriers. *IEEE Transactions on Ultrasonics, Ferroelectrics, and Frequency Control*, *67*(9), 1946–1952. https://doi.org/10.1109/TUFFC.2020.2989667

Guvenc, I., Sahinoglu, Z., & Orlik, P. V. (2006). TOA estimation for IR-UWB systems with different transceiver types. *IEEE Transactions on Microwave Theory and Techniques*, *54*(4), 1876–1886. https://doi.org/10.1109/TMTT.2006.872044

Kay, S. M. (1993). *Fundamentals of statistical signal processing, estimation theory, volume I.* Prentice Hall PTR.

Kazaz, T., Janssen, G. J. M., Romme, J., & van der Veen, A.-J. (2021). Delay estimation for ranging and localization using multiband channel state information. *IEEE Transactions on Wireless Communications.* https://doi.org/10.1109/TWC.2021.3113771

Koelemeij, J. C. J., Dun, H., Diouf, C. E. V., Dierikx, E. F., Janssen, G. J. M., & Tiberius, C. C. J. M. (2022). A hybrid optical-wireless network for decimetre-level terrestrial positioning. *Nature, 611 (7936),* 473–478. https://doi.org/10.1038/s41586-022-05315-7

Kulmer, J., Hinteregger, S., Großwindhager, B., Rath, M., Bakr, M. S., Leitinger, E., & Witrisal, K. (2017). *Proc. of the IEEE International Conference on Communications Workshops, WT03 Workshop on Advances in Network Localization and Navigation (ICC Workshops 2017),* Paris, France. https://doi.org/10.1109/ICCW.2017.7962828

Li, H., Gong, G., Pan, W., Du, Q., & Li, J. (2015). Temperature effect on White Rabbit timing link. *IEEE Transactions on Nuclear Science*, *62*(3), 1021–1026. https://doi.org/10.1109/TNS.2015.2425659

Li, H., Han, L., Duan, R., & Garner, G. (2017). Analysis of the synchronization requirements of 5G and corresponding solutions. *IEEE Communications Standards Magazine*, *1*(1), 52–58. https://doi.org/10.1109/MCOMSTD.2017.1600768ST

Li, Y., & Stuber, G. (2006). *Orthogonal frequency division multiplexing for wireless communications.* Springer Science & Business Media. https://doi.org/10.1007/0-387-30235-2

Lipinski, M. M. (2016). *Vol. 40 - methods to increase reliability and ensure determinism in a White Rabbit network* [Doctoral Thesis, Warsaw University of Technology]. (No. CERN-THESIS-2016-283). https://cds.cern.ch/record/2261452?ln=en

Lopez, O., Haboucha, A., Kéfélian, F., Jiang, H., Chanteau, B., Roncin, V., Chardonnet, C., Amy-Klein, A., & Santarelli, G. (2010). Cascaded multiplexed optical link on a telecommunication network for frequency dissemination. *Optics Express*, *18*(16), 16849–16857. https://doi.org/10.1364/OE.18.016849

Moreira, P., Serrano, J., Wlostowski, T., Loschmidt, P., & Gaderer, G. (2009). White Rabbit: Sub-nanosecond timing distribution over Ethernet. *Proc. of the International Symposium on Precision Clock Synchronization for Measurement, Control and Communication.* Brescia, Italy. https://doi.org/10.1109/ISPCS.2009.5340196

Morton, Y. J., van Diggelen, F., Spilker Jr, J. J., Parkinson, B. W., Lo, S., & Gao, G. (2021). *Position, navigation, and timing technologies in the 21st century: Integrated satellite navigation, sensor systems, and civil applications* (Vol. 1 and 2). Wiley-IEEE Press.

Muljadi, E., Zhang, Y. C., Allen, A., Singh, M., & Gevorgian, V. (2014). *Technical report: Synchrophasor applications for wind power generation* (Tech. Rep. No. NREL/TP-5D00-60772).

Nuijts, R. J. M.W., & Koelemeij, J. C. J. (2016). *System and method for network synchronization and frequency dissemination.* (U.S. Patent No. 9,331,844). Google Patents. https://patents.google.com/patent/US9331844B2/ja

Peek, H., & Jansweijer, P. (2018). White Rabbit absolute calibration. *Proc. of the IEEE International Symposium on Precision Clock Synchronization for Measurement, Control, and Communication (ISPCS 2018),* Geneva, Switzerland. https://doi.org/10.1109/ISPCS.2018.8543067

Pozyx, N.V. (2020). http://www.pozyx.io/. [online, accessed June 2022]

Prager, S., Haynes, M. S., & Moghaddam, M. (2020). Wireless subnanosecond RF synchronization for distributed ultrawideband software-defined radar networks. *IEEE Transactions on Microwave Theory and Techniques*, *68*(11). https://doi.org/10.1109/TMTT.2020.3014876

Progri, I., Bromberg, M., & Michalson, W. (2005). Maximum-likelihood GPS parameter estimation. *NAVIGATION*, *52*(4), 229–238. https://doi.org/10.1002/j.2161-4296.2005.tb00365.x

Riley,W. (2018). *Handbook of frequency stability analysis.* NIST Special Publication 1065. https://tf.nist.gov/general/pdf/2220.pdf

Rizzi, M., Lipinski, M., Ferrari, P., Rinaldi, S., & Flammini, A. (2018). White Rabbit clock synchronization: Ultimate limits on close-in phase noise and short-term stability due to FPGA implementation. *IEEE Transactions on Ultrasonics, Ferroelectrics, and Frequency Control*, *65*(9), 1726–1737. https://doi.org/10.1109/TUFFC.2018.2851842

Rizzi, M., Lipiński, M., Wlostowski, T., Serrano, J., Daniluk, G., Ferrari, P., & Rinaldi, S. (2016). White Rabbit clock characteristics. *Proc. of the IEEE International Symposium on Precision Clock Synchronization for Measurement, Control, and Communication (ISPCS 2016),* Stockholm, Sweden. 1–6. https://doi.org/10.1109/ISPCS.2016.7579514

Ruiz, A. R. J., & Granja, F. S. (2017). Comparing Ubisense, BeSpoon, and DecaWave UWB location systems: Indoor performance analysis. *IEEE Transactions on Instrumentation and Measurement*, *66*(8), 2106–2117. https://doi.org/10.1109/TIM.2017.2681398

Sadlier, G., Flytkjær, R., Sabri, F., & D., H. (2017). *The economic impact on the UK of a disruption to GNSS*. London Economic, report commissioned by Innovate UK.

Serrano, J., Lipinski, M., Wlostowski, T., Gousiou, E., van der Bij, E., Cattin, M., & Daniluk, G. (2009). The White Rabbit project. *Proc. of the 12th International Conference on Accelerator and Large Experimental Physics Control Systems (ICALEPCS 2009),* Kobe, Japan. https://accelconf.web.cern.ch/icalepcs2009/papers/tuc004.pdf

Shamaei, K., & Kassas, Z. M. (2018). LTE receiver design and multipath analysis for navigation in urban environments. *NAVIGATION*, *65*(4), 655–675. https://doi.org/10.1002/navi.272

Śliwczyński, Ł., Krehlik, P., Czubla, A., Buczek, Ł., & Lipiński, M. (2013). Dissemination of time and RF frequency via a stabilized fibre optic link over a distance of 420 km. *Metrologia*, *50*(2). 133–145. https://doi.org/10.1088/0026-1394/50/2/133

Smets, R. (2016). *Engineering rules for bi-directional photonic transport White-Rabbit time and frequency transfer service on existing in-service infrastructure* (Tech. Rep. No. ASTERICS-H2020-653477 – Report D5.1).

Sotiropoulos, N., Okonkwo, C., Nuijts, R., De Waardt, H., & Koelemeij, J. (2013). Delivering 10 Gb/s optical data with picosecond timing uncertainty over 75 km distance. *Optics Express*, *21*(26), 32643–32654. https://doi.org/10.1364/OE.21.032643

Teunissen, P. J. G., & Montenbruck, O. (2017). *Springer handbook of Global Navigation Satellite Systems*. Springer Verlag. https://doi.org/10.1007/978-3-319-42928-1

The Green Village. (2021). https://www.thegreenvillage.org/. [online, accessed June 2022]

The Royal Academy of Engineering. (2011). *Global navigation space systems: reliance and vulnerabilities.* https://raeng.org.uk/media/5shgtv4t/global-navigation-space-systems.pdf

Vasisht, D., Kumar, S., & Katabi, D. (2016). Decimeter-level localization with a single WiFi access point. *Proc. of the 13th USENIX Symposium on Networked Systems Design and Implementation (NSDI '16),* Santa Clara, CA. https://www.usenix.org/system/files/conference/nsdi16/nsdi16-paper-vasisht.pdf

Widrow, B. (2016). *Simultaneous two-way transmission of information signals in the same frequency band.* (U.S. Patent Application US2007/0173195 A1) https://image-ppubs.uspto.gov/dirsearch-public/print/downloadPdf/20020032004

Yan, J., Tiberius, C. C., Teunissen, P. J., Bellusci, G., & Janssen, G. J. (2010). A framework for low complexity least-squares localization with high accuracy. *IEEE Transactions on Signal Processing*, *58*(9), 4836–4847. https://doi.org/10.1109/TSP.2010.2050313

Yavari, M., & Nickerson, B. G. (2014). *Ultra wideband wireless positioning systems* (Tech. Rep. TR14-230). Faculty of Computer Science, University of New Brunswick, Fredericton, Canada. https://www.cs.unb.ca/tech-reports/documents/TR14-230.pdf